Self-aggregating Tau Fragments Recapitulate Pathologic Phenotypes and Neurotoxicity of Alzheimer's Disease in Mice

Ly Thi Huong Luu Le[1,2]†, Jeeyoung Lee[1,2]†, Dongjoon Im[3]†, Sunha Park[2]†, Kyoung-Doo Hwang[2,4]†, Jung Hoon Lee[1], Yanxialei Jiang[1,5], Yong-Seok Lee[2,4,6]*, Young Ho Suh[2,6]*, Hugh I. Kim[3]*, and Min Jae Lee[1,2,7]*

[1]Department of Biochemistry and Molecular Biology, Seoul National University College of Medicine, Seoul 03080, Korea

[2]Department of Biomedical Sciences, Seoul National University Graduate School, Seoul 03080, Korea

[3]Department of Chemistry, Korea University, Seoul 02841, Republic of Korea

[4]Department of Physiology, Seoul National University College of Medicine, Seoul 03080, Korea

[5]School of Medicine, Linyi University, Linyi 276000, China

[6]Neuroscience Research Institute, Seoul National University College of Medicine, Seoul 03080, Korea

[7] Ischemic/Hypoxic Disease Institute, SNU Dementia Research Center, Seoul National University College of Medicine, Seoul 03080, Korea

†These authors contributed equally to this work.

*Correspondence should be addressed to M.J.L. (minjlee@snu.ac.kr), Y.H.S (suhyho@snu.ac.kr), H.I.K. (hughkim@korea.ac.kr), and Y.S.L. (yongseok7@snu.ac.kr)

Keywords: tau, Alzheimer's disease, aggregation, phosphorylation, axon initial segment.

ABSTRACT

In tauopathic conditions, such as Alzheimer's disease (AD), highly soluble and natively unfolded tau polymerizes into an insoluble filament; however, the mechanistic details of this process are not clear. In AD brains, only a small segment of tau forms β-helix-stacked protofilaments, while its flanking regions form disordered fuzzy coats. Here, we demonstrated that the tau AD nucleation core (tau-AC) sufficiently induced self-aggregation and recruited full-length tau to filaments. Unexpectedly, phospho-mimetic forms of tau-AC (at Ser324 or Ser356) showed markedly reduced aggregation and seeding propensities. Biophysical analysis revealed that the N-terminus of tau-AC facilitated the fibrillization kinetics, while its phosphorylation induced conformation changes, sterically shielding the nucleation motif. Tau-AC oligomers were efficiently internalized into cells via endocytosis and induced endogenous tau aggregation. In primary hippocampal neurons, tau-AC impaired axon initial segment plasticity upon chronic depolarization and was mislocalized in the somatodendritic compartments. Furthermore, we observed significantly impaired memory retrieval in mice intrahippocampally injected with tau-AC fibrils, which corresponded to the neuropathological staining and neuronal loss in the brain. These findings identified tau-AC species as a key neuropathological driver in AD, suggesting novel strategies for therapeutic intervention.

INTRODUCTION

Filamentous tau inclusions in neurons are the pathological hallmark of a broad class of neurodegenerative diseases collectively called tauopathies. These disorders can be further classified into primary tauopathies, such as corticobasal neurodegeneration, where tau aggregation is the predominant molecular lesion, and secondary tauopathies, which have aggregates of additional proteins, including the most prevalent Alzheimer's disease (AD).[1] Microtubule-associated protein tau is encoded by *MAPT* gene, generating multiple isoforms via alternative splicing.[2] The longest tau isoform (2N4R, 441 residues) contains four functional domains: an N-domain, proline-rich domain, microtubule-binding domain (MBD), and C-terminal region (Fig. 1A), resulting in a highly soluble (average hydropathicity of –0.87) and positively charged protein (net pI = 8.2).[3] The four repeats (R1–R4) in the MBD were originally believed to be critical for forming β-sheet-rich straight or paired helical filaments (SFs or PHFs, respectively);[4] however, recent cryoelectron microscopy (cryo-EM) studies showed that insoluble tau filaments contained only R3, R4, and a part of the C-terminal region.[5] Having the anti-parallel C-shaped stacks of the segments, the secondary structures of SFs and PHFs from human brains with AD were analogous.[6] Furthermore, the recombinant tau fragments, consisting of 2N4R tau residues 306–378 (hereafter named tau-AC), spontaneously assembled and further induced endogenous tau aggregation.[7] However, the underlying mechanisms driving this phenomenon and its pathophysiological implications in AD remain largely uncharacterized.

Recent evidence indicates that post-translational modifications (PTMs) are critical in the self-aggregation of otherwise soluble tau.[8] After hyperphosphorylated tau species were identified in human AD brains in 1986,[9] phosphorylation has been considered the central event in tau

fibrilization.[10] More than 85 phosphorylatable residues were reported in 2N4R tau (~19% of all amino acids).[11] Several drugs were developed based on this etiological concept; however, they showed essentially no therapeutic effect in clinical trials.[12] A study combining cryo-EM and mass spectrometric analysis reported that, while some residues of tau-AC were phosphorylated, its inter-filament packing was stabilized by multiple polyubiquitin chains on Lys residues, providing more interfacial contacts.[6] This model was consistent with previous biochemical studies showing that tau phosphorylation initially promoted its ubiquitylation for proteasomal degradation, eventually resulting in tau hyperubiquitylation and insoluble protofilaments (a "double-hit" model).[3] Several studies reported that tau acetylation, which potentially competes with ubiquitylation at the same Lys residues, augments pathologic tau aggregation.[13, 14] Therefore, the pathological consequence of tau PTMs needs to be further clarified.

Tau proteins predominantly reside in the axons of mature neurons, contributing to microtubule stabilization and axonal transport, as well as synaptic plasticity and neuronal excitability.[15, 16] AD neurons lose their tau polarization, leading to tau accumulation in the soma and dendrites.[17, 18] Pathologic forms of tau detached from microtubules are transported to somatodendritic compartments through the axon initial segment (AIS) located near the hillock of axons with 20–60 μm length. The AIS serves as a diffusion barrier and a selective filter, which sorts the axonal and somatodendritic proteins.[19] The AIS cytoskeleton consists of submembrane proteins, cytoskeletal proteins, and filamentous actin (F-actin).[20] The AIS is also critical for neuronal excitability, since it is enriched with voltage-gated ion channels and initiates axon potential (AP) firing.[21, 22] In addition, the anatomical characteristics of the AIS, including its position and length, are dynamically regulated under physiological and pathological conditions.[23] Pathologic tau is localized to dendritic spines to a much greater extent than to dendritic shafts

through directly interaction with F-actin and affects the AIS cytoskeleton and plasticity, implicated in AD and other tauopathies.[24, 25]

Since the intracellular events leading to tau fibrillization are not fully understood, it is critical to identify the pathological forms of tau species. In this study, we demonstrated that tau-AC efficiently self-assembled and triggered the co-aggregation of normal tau. These biochemical characteristics of tau-AC were diminished in Ser324 and Ser356 pseudo-phosphorylated tau-AC (phospho-tau-AC). Using biophysical analysis, we identified a possible mechanism of substantial aggregation propensity and seeding capacity of tau-AC, as well as its conversion into pathologically inactive phospho-tau-AC. Oligomeric tau-AC was internalized by cultured cells and primary hippocampal neurons, primarily via caveolin-mediated endocytosis, triggering endogenous tau aggregation. Isolated primary neurons infected with tau-AC-expressing lentiviruses demonstrated significantly shortened axon initial segment (AIS) in response to chronic depolarization and mislocalized tau in dendritic spines, which collectively implicated synaptic dysfunction. Finally, we stereotaxically injected tau-AC into the mouse hippocampus and found that these mice had significantly increased levels of histopathological staining, altered anxiety-like behavior, and impaired contextual fear memory retrieval compared to the animals injected with phospho-tau-AC. Collectively, our findings provide the molecular insight into the causal mechanism of AD and identify novel therapeutic strategies targeting the cleavage and phosphorylation of tau.

RESULTS

Self-assembling and seeding properties of tau-AC *in vitro*

To investigate the self-aggregation and seeding properties of tau-AC, we first purified the full-length 2N4R human tau (tau-FL), as well as its truncated form containing amino acids 306 to 378 (tau-AC) (Fig. 1A). Tau-AC gradually generated high-molecular weight species after ~1-day incubation with gentle shaking at 37°C without anionic cofactors, such as heparin or dextran sulfate (Fig. 1B). When co-incubated with tau-FL, tau-AC induced the oligomerization of tau-FL, as demonstrated by immunoblotting analysis using TAU-5 and TAU-AC antibodies specifically targeting tau-FL and tau-AC, respectively (Fig. 1C). In the absence of tau-AC, tau-FL did not generate any oligomeric species for up to 3 days. We also observed the formation of heterotypic oligomers consisting of both tau-FL and tau-AC (Fig. S1A). The seeding effect of tau-AC appeared to be stoichiometric: equimolar tau-FL and tau-AC were effectively co-aggregated while a 0.5:1 or lower molar ratios of tau-AC to tau-FL resulted in only minor aggregation (Fig. S1B and S1C). To directly evaluate tau fibrillization, we performed a filter trap assay and observed that highly soluble tau-FL became trapped in the membrane when pre-incubated with tau-AC (Fig. 1D). The insoluble and oligomeric tau-FL species were also retrieved from the pellet fractions of ultracentrifuged samples that were pre-incubated with tau-AC (Fig. S1D).

Thioflavin T (ThT) intensity, which corresponds to the presence of β-sheet structures in filaments, was gradually increased when tau-FL was incubated with tau-AC; however, the signal was virtually absent in samples containing only tau-FL (Fig. 1E). Tau-AC alone generated stronger ThT signal than the combination of tau-FL and tau-AC, further indicating its prominent self-aggregation ability. To verify these findings, samples evaluated by negative-staining transmission

electron microscopy (TEM) at the 48-h reaction point (Fig. 1F). Tau-FL generated a large number of fibrils only in the presence of heparin, while tau-AC spontaneously formed distinct fibrils. The morphology of tau-AC was significantly shorter and thicker than the filament bundles of heparin-induced tau-FL (Fig. 1G). The short and thick fibrils of tau-AC could function as effective protofilamental nucleates for further self-aggregation and recruitment of endogenous tau-FL into fibrils. As expected, tau-FL effectively stabilized microtubules, as assessed by tubulin oligomerization and sedimentation assays (Fig. 1H and 1I). In sharp contrast, we observed that tau-AC had a much weaker binding affinity to tubulins than tau-FL, also marginally facilitating microtubule assembly (Fig. 1H and 1I). Collectively, these data suggest that tau-AC, which is not associated with microtubules, has an intrinsic ability to form pathologic aggregates *in vitro* even without aggregation inducers or PTMs.

Antagonistic effects of tau-AC phosphorylation on the self-aggregation and seeding

The majority of tau phosphorylation occurs at the residues located outside of the MBD and this is considered to be an early pathologic event in AD.[26] Using an *in vitro* phosphorylation reaction and MS analysis, we identified two phosphorylation sites, Ser324 and Ser356, in tau-AC; both sites contained the Lys-Ile-Gly-Ser motif in the R3 and R4 repeats, respectively (Fig. 2A).[3] Unexpectedly, tau-AC, which was phosphorylated with recombinant GSK3β, showed much weaker self-aggregation than intact tau-AC (Fig. S2A). To further investigate the consequences of site-specific phosphorylation, we purified wild-type tau-AC (tau-AC-wt) and its phospho-mimetic point mutants (phospho-tau-AC; S324D, S356D, and S324D/S356D [SDSD]), and performed the *in vitro* self-assembly assay. Unlike aggregation-prone tau-AC-wt, the phospho-tau-AC species showed a significantly reduced level of oligomerization (Fig. 2A). Tau-AC-S356D showed a more

prominent decrease in oligomerization than tau-AC-S324D. Consistent with these results from gel-based assays, the filter trap analysis demonstrated that pseudo-phosphorylation mutants, especially tau-AC-S356D, had drastically reduced self-aggregation (Fig. 2B). After ultracentrifugation, tau-AC-wt, but not its phospho-mimetic forms, remained predominantly in the pellet fraction along with tau-FL, confirming that phosphorylation interfered with the seeding ability of tau-AC (Fig. 2C). Collectively, these results indicate that the phosphorylation in tau-AC may affect its fibrillization kinetics and function as an antagonistic mechanism of tau aggregation.

To investigate the mechanism underlying the biochemical properties of tau-AC species, we first performed structural analysis using small-angle X-ray scattering (SAXS). The Kratky analysis of the SAXS profiles and circular dichroism (CD) spectra indicated that both wild-types and phospho-mimetic mutants of tau-AC were largely unstructured and random-coiled (Fig. S2B and S2C). The experimental radius of gyration (R_g) values from the SAXS profiles indicated that the relatively extended tau-AC-wt (27.25 ± 0.30 Å) became more compact after phosphorylation (25.20 ± 0.70, 24.33 ± 0.84, and 24.72 ± 1.01 Å for tau-AC-S324D, -S356D, and -SDSD mutants, respectively) (Fig. 2D). Next, we performed the ensemble optimization method (EOM) analysis of the X-ray scattering patterns, combined with replica-exchange molecular dynamics (REMD) simulations. The resulting conformation pools of each tau-AC species revealed that the phospho-mimetic mutants had a more compact structure than tau-AC-wt, confirming the results of R_g analysis (Fig. 2E and 2F). The extended conformer distribution of tau-AC-wt was centered at 34.52 Å, while the distribution of pseudo-phosphorylation mutants was 28.93, 30.11, and 31.00 Å for S324D, S356D, and SDSD, respectively. We also found that the N-terminal residues of tau-AC, containing the hexapeptide motif ^{306}VQIVYK^{311} (also known as the PHF6 motif),[27] had the lowest solubility scores (< -1) (Fig. S2D). Our calculated conformations suggested that the PHF6 motif

of tau-AC-wt and tau-AC-S324D were highly accessible for oligomerization; in contrast, those of tau-AC-S356 and tau-AC-SDSD mutants were largely sterically shielded (Fig. 2F). Taken together, we postulated that the N-terminally exposed PHF motif might function as the crucial contact points between tau-AC monomers for their self-aggregation. In addition, tau-AC phosphorylation might induce a conformational change through enhanced intramolecular electrostatic interactions, which brings the N-termini inward and obstructs their interactions.

The structural properties of tau-AC and its phospho-mimetic mutants were further analysed using electrospray ionization/ion mobility mass spectrometry (ESI-IM-MS). The IM spectra also indicated that tau-AC-wt and -S324D had an extra population with extended conformations, whereas tau-AC-S356D and -SDSD mutants only showed compact conformations (Fig. 2G and Fig. S2E). To gain a mechanistic insight into the interpeptide interactions, we next performed an *in silico* analysis of tau-AC dimers by running all-atom REMD simulations sets consisted of 76 different temperatures ranging from 300 to 400 K with equal exchange probabilities. The obtained contact maps from equilibrated trajectories revealed that tau-AC-wt retained strong dimeric interactions via the ^{306}VQIVYK^{311} hexapeptide motifs at the N-terminus, while the tau-AC-SDSD mutant demonstrated significantly weakened interchain interactions (Fig. 2H and Fig. S2F). The contact probability maps of tau-AC-wt and -SDSD double mutant showed global differences, indicating a significant change in the three-dimensional structures as a result of tau-AC phosphorylation. Finally, we carried out the *in vitro* aggregation reactions with other tau-AC mutants, which either lacked the PHF6 motif (tau-AC-ΔPHF6) or had it substituted with hydrophilic residues (tau-AC-TQDVSK), and found that, unlike tau-AC-wt, these mutants fail to self-assembled or to induce tau-FL aggregation (Fig. S3A – S3E). Therefore, the hydrophobic interactions between the N-terminal motifs appeared to play a nucleating role at the early stage of

tau-AC aggregation. Moreover, our integrated biophysical and biochemical data suggested that phosphorylation-mediated structural changes from extended to compact forms might interfere with the interactions between the PHF6 motifs. Consistent with this, whereas phospho-Ser202/Ser205-tau levels (detected by AT8 antibodies) in transgenic AD model mouse brains were elevated from age-matched wild-type controls, the level of phospho-S356-tau were significantly reduced (Fig. 2I).

Cellular uptake of tau-AC aggregates and its effect on endogenous tau

Next, we examined whether the spontaneously aggregated tau-AC species would be internalized by cells similar to other aggregation-prone proteins, such as amyloid β peptides,[28] prion proteins,[29] and huntingtin with expanded polyglutamine repeats.[30] A549 cells and primary hippocampal neurons were treated with FLAG-tagged monomeric (0 day of assembly reaction) and oligomeric (2 days) tau-AC, respectively, vigorously washed, and then replated after trypsinization to completely remove the membrane-bound tau-AC. Immunostaining using anti-FLAG antibodies demonstrated intracellular inclusions localized on the same Z-stack plane as α-tubulin and DAPI (Fig. 3A and Fig. S4A). We observed that internalized tau-AC puncta were found in ~25% of cells treated with oligomeric tau-AC; however, no tau-AC-positive inclusions were detected in monomeric tau-AC-treated cells (Fig. 3A). In primary neurons, the majority of tau-AC signals were observed in the soma, while a small number of punctate signals was also detected in the axons (Fig. S4A and S4B). Further analysis revealed that tau-AC aggregates were primarily localized in the endosomes and lysosomes, as identified by co-immunostaining with Rab5, Rab7, and LAMP1 antibodies (Fig. S4C). Since the majority of intracellular tau-AC appeared to be trafficked to the downstream compartments of the endocytic transport system, we tested several endocytosis

inhibitors. Our results showed that genistein (caveolin-mediated endocytosis inhibitor) reduced tau-AC internalization, while amiloride (a macropinocytosis inhibitor) had little effect (Fig. 3B). Chlopromazine, a clathrin-mediated endocytosis inhibitor, also decreased the cellular uptake of tau-AC, but to a lesser degree. These data suggested that the oligomeric species of tau-AC, but not its monomeric form, are actively internalized through caveolin-mediated endocytosis, rather than passive transmembrane diffusion.

Next, we examined whether internalized tau-AC stimulated the aggregation of endogenous tau using HEK293 tau-P301S biosensor (tau-FRET) cells, which generate Förster resonance energy transfer (FRET) signals in response to tau-CFP and -YFP polymerization.[31] Upon the exposure of the tau-FRET cells to oligomeric forms of tau-AC, the FRET signal was dramatically increased compared to the negligible background signal (Fig. 3C). In addition, these effects were proportional to the amount of tau-AC oligomers presented to the tau-FRET cells (Fig. S4D). At the same time, similar to the tau-AC internalization results, monomeric tau-AC did not produce any detectable FRET signals. Thus, the seeding ability of tau-AC selectively corresponded to the pathological aggregates in live cells. To further confirm these findings, we cloned tau-AC into a vector that included an N-terminal-fused NS3 protease with its own cleavage site at the junction between NS3 protease and tau-AC (Fig. 3D). Upon transient overexpression of this construct with tau-FL, the high-molecular weight species of both tau-FL and tau-AC were observed in the pellet fractions in the presence of the proteasome inhibitor MG132 (Fig. 3D), providing further evidence of tau-AC seeding ability.

We also investigated the effect of tau-AC phosphorylation on endogenous tau aggregation in cells. In tau-FRET cells, virtually no FRET signal or tau puncta were detected in cells treated with tau-AC-S324D, -S356D, and -SDSD mutants, which was in stark contrast to tau-AC-wt-

treated cells (Fig. S4E). To confirm these observations, primary cortical neurons were infected with lentivirus expressing diverse tau-AC constructs, and IB analysis using whole-cell lysates was performed. Our results indicated that cells expressing tau-AC-wt contained significantly more oligomeric forms of endogenous tau-FL than cells expressing phospho-mimetic tau-AC (Fig. 3E). Similarly, A594 cells treated with tau-AC-S324D and -S356D did not generate noticeable punctate or aggregate signals (Fig. S4F). Taken together, our cell studies largely recapitulated the *in vitro* experiments demonstrating tau-AC's seeding ability and its phosphorylation delaying self-fibrillization.

Tau-AC impaired AIS plasticity and polarized trafficking in neurons

Since tau-AC did not bind to tubulin but interacted with end-binding protein 3 (EB3), a microtubule plus-ending protein and a structural component of the AIS (Fig. 1H and S3F), we hypothesized that overexpression of tau-AC would dominant-negatively impair microtubule dynamics and AIS plasticity. First, we examined differences in the localization and length of the AIS in response to changes in neuronal activity. Dissociated hippocampal neurons were treated with 15 mM extracellular potassium ion (K^+) from 12 to 14 DIV, and the AIS was immunostained for the essential AIS scaffolding protein ankyrin G (AnkG). Similar to a previous report,[32] chronic depolarization using K^+ relocated the AIS distally 4–5 μm down the axon; however, all start, maximum, and end positions were simultaneously shifted, leaving the AIS length unchanged (Fig 4A). The primary function of the AIS relocation is to modulate downregulated neuronal excitability and upregulate AP spike threshold.[32] In response to overexpression of tau-FL under basal conditions, we observed a significant distal shift of the AIS end positions but no changes in start and max positions, consequently increasing the AIS length (Fig. 4A). The lengthening of AIS

by tau-FL was effectively reversed upon chronic depolarization by proximal translocation of the AIS end points, suggesting that neurons expressing tau-FL partially mimicked the effect of hyperphosphorylated tau-E14 expression in steady states,[33] but still retained activity-dependent AIS plasticity. In contrast, neurons overexpressing tau-AC did not respond to the prolonged K^+ signal, showing little changes in the AIS position (Fig. 4A). These data indicated that the AIS plasticity was severely impaired by tau-AC, providing a possible explanation for neuronal network hyperexcitability and excitotoxicity observed in various AD mouse models.[34] By monitoring additional AIS markers EB3 and βIV-spectrin, we also observed similar consequences: a significant shortening of the AIS length in response to tau-AC (Fig. 4B). Therefore, the entire AIS compartments were misregulated by overexpressed tau-AC.

Since AIS plasticity determines not only AP initiation but also the polarized trafficking of tau from the soma to axon, we next investigated the localization of overexpressed tau-AC in primary neurons. We co-transfected hippocampal neurons with EGFP-tagged tau-FL or tau-AC with tandem dimer Tomato (tdTomato), which was used to normalize the axon-to-dendrite distribution because it is uniformly distributed across axons and dendrites. We detected tau-FL was primarily localized in axons rather than dendritic branches (Fig. 4C). In contrast, a significant fraction of tau-AC was mislocalized to the somatodendritic compartment (Fig 4C), suggesting that the selective filtering function of the AIS was disrupted by overexpressed tau-AC. We also evaluated whether mislocalized tau-AC changed synaptic function by affecting the number of dendritic spines. Tau-AC and tdTomato double-labeling showed that tau-AC only modestly decreased the number of dendritic spines (Fig 4D), suggesting that intraneuronal expression of tau-AC by itself did not significantly induce acute synapse loss. However, the number of tau-AC-positive dendritic spines was significantly higher than that of tau-FL-positive spines (Fig 4D),

implicating that tau-AC could cause synaptic dysfunction in dendritic spines.[35] Taken together, these findings demonstrate that tau-AC-driven pathological processes in neurons include impaired AIS plasticity and tau mislocalization.

Behavioral phenotypes and neuronal death induced by tau-AC in mice

To test whether tau-AC can recapitulate AD or tauopathy phenotypes in young (3-month old) non-transgenic mice, we stereotaxically injected preformed fibrils of either tau-AC-wt or pseudo-phosphorylated tau-AC-S356D unilaterally into the hippocampus (Fig. 5A and Fig. S5A).[36] To evaluate tau-AC-mediated pathology, we performed immunostaining on the series of coronal sections near the injection site and observed a stronger tau-AC-wt signal in the hippocampus than tau-AC-S356D (Fig. 5B and 5C; Fig. S5B). Abundant tau-AC staining was largely confined to the injection coordinates of the ipsilateral hippocampus but a small fraction could also be detected in the anterior and posterior regions. Double staining demonstrated that the high level of tau-AC signal was associated with the loss of NeuN signal (Fig. 5B and 5C). No tau pathology, such as tau filaments, neuronal loss, or inflammation, was observed in control mice. Furthermore, we could detect filamentous tau filaments in the mouse brains injected with tau-AC-wt using anti-tau antibodies AT-8 and T22, both of which detect the pathological forms of endogenous tau, but not exogenous tau-AC (Fig. S5C and S5D). AT-8- or T22-positive neurons were also largely colocalized with strong FLAG immunoreactivity, which corresponded to tau-AC aggregates. At the same time, the tau-AC-S356D mutant failed to induce tau aggregation after the intra-hippocampal injection (Fig. S5C and S5D), suggesting that tau-AC phosphorylation plays an antagonistic role in self-nucleation and seeding in mice as well.

To confirm these findings, we performed histochemical staining using thioflavin S (ThS),

which allows the visualization of mature tau tangles. We observed a distinct ThS-positive signal in the CA1 region of the hippocampus in mice injected with tau-AC-wt fibrils, while the ThS-signal was significantly lower in mice injected with tau-AC-S356D (Fig. S5E). Using the TUNEL assay, we observed that the high intensity tau-AC-positive signal was preferentially overlapped with apoptotic neurons (Fig. 5D), providing a possible link between the observed neuronal loss and memory impairment in tau-AC-injected mice. Beside this relatively selective loss of CA1 neurons, the gross morphology of tau-AC-injected mice was highly comparable to controls. Although we did not observe tau-AC staining in the contralateral, non-injected hippocampus (Fig. S5G), pathologic tau species appeared to be spatially propagated to the frontal cortex of the ipsilateral hemisphere (Fig. S5C and S5E). Intriguingly, tau-AC-wt-injected mice showed extensive GFAP staining near the CA1 region (Fig. 5E). These results suggest that tau-AC, as a potent causal agent of tauopathies, could also induce neuroinflammation and astrogliosis, which are early signals of AD progression and, potentially, protection mechanisms of the brain against pathogenic tau species.

Next, mice were evaluated for their basal locomotor activity and anxiety-like behavior using an open field test. Mice from both tau-AC-wt and -S356D groups had moving distances similar to the control mice, indicating that their locomotive functions were unaffected. At the same time, tau-AC-wt-injected mice spent significantly longer time in the peripheral region than controls, thus suggesting a tendency for anxiety-like behaviors, while mice injected with tau-AC-S356D showed no significant changes in the open field test (Fig. 5F). To evaluate their learning and memory functions, mice were subjected to a classical fear conditioning test, which is a form of Pavlovian-associative learning. Two months after the injection, mice were trained with pairing of acoustic tone and electric shock, where all groups showed similar freezing behaviors in response

to baseline, tones, and inter-tone intervals during the conditioning session (Fig. 5G, *left*). The next day, mice were exposed to the same conditioning chamber to test their fear memory, which is dependent on the hippocampus.[36] In contextual fear memory, tau-AC-wt-injected mice displayed a significantly lower freezing times than control mice (Fig. 5G, *middle*). Of note, mice injected with tau-AC-S356D showed freezing times comparable to the controls. In auditory fear memory retrieval test, however, the freezing level of tau-AC-wt-injected mice was only mildly reduced from those of the other groups, suggesting that the tau-AC-induced memory deficit appear to be restricted to the hippocampal test (Fig. 5G, *right*). These data collectively suggest that tau-AC, but not phosphorylated tau-AC, has a clear capacity to induce behavioral deficit, including anxiety-like behavior and hippocampal memory impairment, along with neuropathological phenotypes and neurotoxicity.

DISCUSSION

Considerable efforts have been made to identify the key molecular mechanism involved in tau aggregation. Increasing evidence suggests that tau proteins are often cleaved by multiple proteases, including calpains, caspases, and endopeptidases, and these tau fragments have pro-fibrillizing and seeding properties if not properly degraded.[37] Numerous studies have also suggested that R3 and R4 repeats of tau are essential for its pathological role, while the flanking regions may not be required or could even serve a protective role by preventing tau aggregation.[38-40] Based on our *in vitro* and *in vivo* assays, we demonstrated that 2N4R tau residues 306–378 (tau-AC) were the sufficient and essential fragment for the initiation of self-amplifying cascades (Fig. 1A – 1G). In addition, we found that tau-AC lacking the R1 and R2 repeats of the MBD was unable to bind to tubulin or facilitate microtubule assembly (Fig. 1H and 1I). Thus, the four tandem repeats of the MBD may play different roles in the formation of orderly β-sheet structures of tau. Negatively stained TEM showed that tau-AC fibrils had a different morphology compared to heparin-induced tau fibrils, with significantly thicker and shorter filament bundles, which are favorable to become a protofilamental seed and more physiologically related to human AD tau filaments (Fig. 1F and 1G).[6] Therefore, cleavage events of tau-FL into tau-AC or corresponding fragments may be the critical for the pathogenesis of tauopathies (Fig. 6). Although it remains difficult to identify the exact proteases responsible for the generation of tau fragments, understanding cellular conditions that increase amyloidogenic tau-AC is necessary to provide an insight into AD pathogenesis.

Based on the results of integrative biochemical/biophysical analysis, we propose that the underlying mechanism of tau-AC aggregation depends on the strong intermolecular interactions between the N-termini of R3 repeats, the location of β-sheet forming ^{06}VQIVYK^{311} (PHF6) motifs

(Fig. 2D – 2G). Compared to tau-FL, tau-AC is expected to have increased accessibility and flexibility between the PHF6 motifs, initiating the formation of tau proto-filaments. The majority of mouse lines overexpressing normal tau-FL are reported to have little signs of obvious tau inclusions or neurodegeneration.[41, 42] Therefore, the cleavage of the N-terminal portion of tau functions exposing the PHF6 motif as a prerequisite event and onset signal for generating tau nucleates. It is notable that pseudo-phosphorylation of KxGS motifs in R3 (S324) and R4 (S356) repeats significantly reduced the aggregation propensity of tau-AC (Fig. 2A – 2C). We found that the mutation of S324, S356, or both sites to Asp significantly shifted the global conformation of tau-AC from a relatively extended conformation to a more compact one through electrostatic interactions, shielding the N-termini and limiting the association of the PHF6 motifs. Arakhamia *et al*. reported that the K311 residue of tau is polyubiquitylated in human AD brain.[6] Since polyubiquitin chains can stabilize β-strand stacking, we propose that tau-AC ubiquitylation, unlike phosphorylation, will further facilitate polymeric tau-AC formation. However, the mechanistic link between tau cleavage and its effect on PTM events (or vice versa) during the course of tauopathies remains to be determined. Since the highly heterogeneous nature of tau aggregates makes it challenging to directly target it using conventional small molecules and antibodies, the antagonistic function of tau-AC phosphorylation may provide important insights into designing a novel anti-fibrillogenic therapy to treat tauopathies.

Tauopathies hierarchically progress through the stages, possibly through neuronal connections. For example, in AD, tau lesions accumulate in a defined spatiotemporal pattern: first appearing in the transentorhinal cortex, spreading to anterior hippocampus and adjacent neocortex, and, finally, invading the primary sensory cortex.[43] Missorted tau at somatodendritic compartments can be released into the extra-neuronal space via secretion or other mechanisms.[44]

These findings suggest that intra-neuronal tau proteins, after aggregation, may obtain prion- or β-amyloid-like properties. Our cell culture experiments demonstrated that tau-AC aggregates were transcellularly propagated and the uptake was mediated via endocytic processes (Fig. 3), providing a possible mechanism for the *in vivo* seeding of tau[45, 46] These data also suggest the requirement of a specific extracellular matrix component or even the existence of unidentified tau fibril receptor. Since tau seeds in the extracellular space bind to the cell surface by attaching to heparan sulfate proteoglycans,[47] it is possible that the highly negatively charged proteoglycans may act as receptors (or co-receptors) for tau aggregates and mediate subsequent caveolin-mediated endocytosis. Tau-AC-wt oligomers, but not tau-AC-S356D mutants also functioned as a seed to induce widespread tau pathology after a single injection into the hippocampus (Fig. 5). We observed neuronal death and neuroinflammation mostly around the site of injections but could detect tau aggregates in neighboring cortex regions as well. However, we could not detect inter-lateral tau propagation of tau-AC in mouse brains possibly due to a relatively short time frame (2 months of our animal experiments), which may imply that the slow spreading of pathological tau, rather than its formation, serves as the critical rate-limiting step of AD progression. The pathologic features of tau-AC-injected mouse brains were consistent with previous studies reporting clear correlation between neurofibrillary tangle deposits and cognitive decline.

This current study also demonstrated that tau-AC induced several pathological processes not only in primary neurons (i.e., impaired AIS dynamics and tau trafficking; Fig. 4) and but also in wild- type mice (i.e., defective memory retrieval). We propose that the dysfunctional neuronal excitability (and excitotoxicity as well) in tauopathy model mice could be linked to the impaired AIS dynamics upon activation via tau-AC, which cannot bind to microtubules. However, it remains to be determined whether the defective polarized trafficking of tau we observed originated from

altered interactions between tau-AC and some of AIS elements. In conclusion, we present evidence that tau-AC functions as a strong causal agent in AD, sufficient to induce the essential features of tauopathies, including self-fibrillization, spreading, neurodegeneration, and inflammation. In addition to this pathological relevance, this study also suggests a more efficient and possibly mechanism-modifying strategy for delaying tauopathies by inducing, instead of inhibiting, tau phosphorylation inside the aggregation core.

METHODS

Antibodies and reagents

Antibodies and dilution factors for immunoblotting (IB) and immunofluorescence staining (IF) used in this study were as follows: anti-β-actin (A1978, Sigma, 1/10,000), anti-His (MA1-21315, Thermo Fisher Scientific; 1/2,000), anti-FLAG (PA1-984B, Thermo Fisher Scientific; 1/5,000), anti-tau-AC (polyclonal antibody purified from the tau-AC -immunized rabbit; 1/2,000), anti-tau (clone Tau-5; Invitrogen; 1/5,000 or 1/300 for IF), anti-tau Ser202/Thr205 (AT8 clone; MN1020, Thermo Fisher Scientific; 1/100 for IF), anti-tau Ser356 (ab75603, Abcam; 1/3,000), anti-MAP2 (AB5622, Millipore; 1/500 for IF), anti-NeuN (ab177487, Abcam, 1/500 for IHC), anti-β-tubulin III (MA1-19187, Thermo Fisher Scientific; 1/100 for IF), anti-Rab5 (sc-46692, Santa Cruz; 1/100 for IF), anti-Rab7 (sc-376362, Santa Cruz; 1/100 for IF), anti-LAMP1 (sc-17768, Santa Cruz; 1/100 for IF), anti-GFP (A11122, Thermo Fisher Scientific; 1/300 for IF), mouse anti-AnkG (N106/65, Neuromab; 1/300 for IF), guinea pig anti-AnkG (386-004, Synaptic Systems; 1/300 for IF), anti-βIV-spectrin (N393/76, Neuromab; 1/100 for IF), and anti-EB3 (KT36, ab53360, Abcam, 1/100 for IF). Secondary antibodies for IB (horseradish peroxidase conjugated anti-mouse IgG and anti-rabbit IgG antibodies) were acquired from Millipore. The secondary antibodies for IF (goat anti-rabbit Alexa Fluor 488/594 IgG and goat anti-mouse Alexa Fluor 488/594/647 IgG) were purchased from Thermo Fisher Scientific. The following endocytosis inhibitors were used: genistein (A2198, Apexbio), chlorpromazine (B1480, Apexbio), and amiloride (B1884, Apexbio). Dulbecco's modified Eagle's medium (DMEM), Roswell Park Memorial Institute (RPMI), and fetal bovine serum (FBS) were purchased from WelGENE.

Purification of recombinant tau proteins

To purify tau-FL, tau-AC, and its mutants, *E. coli* strain Rosetta 2 (DE3) cells (Novagen) were grown at 37℃ until the OD at 600 nm reached 0.5. Next, 0.5 mM isopropyl-β-D-thiogalactopyranoside (IPTG) was added to induce tau expression and cells were cultured for 4 h at 37℃. Cells were harvested in a lysis buffer (50 mM phosphate buffer pH 7.0 with protease inhibitor cocktail), lysed using sonication, and then heated for 15 min at 85℃ in a water bath. The precipitates were cleared by centrifugation and filtered through a 0.22 μm polypropylene filter. The resulting supernatant was loaded onto a 5 mL HiTrap Mono S column (GE Healthcare Life Sciences) using the ÄKTA FPLC system (GE Healthcare Life Sciences). The column was then washed with five column volumes of washing buffer (50 mM phosphate buffer pH 7.0) and eluted using a NaCl step-gradient. The eluted proteins were concentrated using Amicon Ultra Centrifugal filters. His-tagged tau-AC was purified using a HiTrap TALON crude column. The elution buffer (50 mM phosphate buffer pH 7.0, 300 mM NaCl, 150 mM imidazole) was passed through TALON column to elute tau-AC protein. Dithiothreitol (DTT) was added to the eluted tau proteins (0.1 mM final concentration) and the proteins were stored at -80℃.

***In vitro* aggregation assay in the presence or absence of heparin**

Tau-FL aggregation was induced using heparin. Briefly, 40 μM of tau-FL was incubated with 80 μM heparin in the assembly buffer (10 mM HEPES pH 7.4, 100 mM NaCl, 1 mM DTT) on a rotating shaker (250 rpm) at 37℃. Tau-AC at 50–100 μM concentration self-aggregated in the assembly buffer (10 mM HEPES pH 7.4, 100 mM NaCl, 1 mM DTT) with gentle shaking (250 rpm) at 37℃. To investigate the seeding effect of tau-AC, 1 mg/mL of tau-FL and 0.2 mg/mL of tau-AC were mixed in the assembly buffer at 37℃ with shaking at 250 rpm.

Filter trap assay, thioflavin T (ThT) assay, and ultracentrifugation analysis

The aggregated tau proteins were mixed with 2× sample buffer (4% SDS, 40 mM EDTA) and were passed through a cellulose acetate membrane (Advantec, 0.2 µM pore size),[48] pre-activated with 0.1% SDS for 5-10 min, using a 96-well dot-blot apparatus (CSL-D96, Cleaver Scientific) with vacuum aspiration. The membrane was washed twice with 200 µL of 0.1% SDS and trapped proteins were analyzed by immunoblotting. For the ThT assay, 4 µM of tau species were incubated with 50 µM of ThT (Sigma) in a reaction buffer (50 mM glycine-NaOH, pH 8.5). The oligomerization kinetics was determined through fluorescence intensity (excitation at 430 nm and emission at 485 nm) at different reaction time points (TECAN infinite M200 fluorometer, Männedorf). After the tau polymerization reaction, samples (100 µL) were centrifuged at 120,000× g for 1 h at 4°C to separate the supernatant and pellet fractions. All samples were resuspended in SDS-sample buffer, heated at 85°C for 10 min, and then subjected to SDS-PAGE/IB.

Microtubules assembly assay

The ability of recombinant tau-FL and tau-AC proteins to accelerate microtubule assembly was evaluated by measuring the fluorescence signal of DAPI (excitation at 358 nm, emission at 461 nm) using TECAN infinite M200 fluorometer (Männedorf). In a final 100 µL volume reaction, 4 mg/mL tubulin (T240, Cytoskeleton) was mixed with either tau-FL or tau-AC (molar ratio tau protein/tubulin = 1/10) in the PEM buffer (80 mM PIPES pH 6.9, 2 mM $MgCl_2$, 1 mM GTP, 10 µM DAPI, and 0.5 mM EGTA). Microtubules assembly was determined by monitoring DAPI fluorescence every 60 sec for 1 h at 37°C. These experiments were performed in triplicate. For tubulin and tau co-sedimentation, the samples were subjected to ultracentrifugation at 68,000× g

for 20 min after the microtubule assembly assay. Pellet and supernatant fractions were analyzed separately using SDS-PAGE.

Transmission Electron Microscopy (TEM) Imaging

To obtain the TEM images of tau-FL and tau-AC fibrils, a negative staining protocol was used. Uranyl acetate (Sigma-Aldrich) stock solution (0.5% (w/v)) was prepared in HPLC grade water (JT Baker) and filtered through a 0.22 μm disposable syringe filter. Tau proteins (40 μM) were incubated for 72 h and then transferred to a 400-mesh formvar/carbon Cu(II) grid (Electron Microscopy Science). The tau fibril samples (5 μL) were spotted on a Cu(II) grid for 3 min at 20℃ and the excess liquid was removed. The grids were washed twice using a 0.5% w/v uranyl acetate solution immediately after removing the samples. Next, each sample was stained with a 5 μL uranyl acetate solution for one minute and dried for 4 h at 20℃. TEM images at several magnifications (200 kV, 6,000×, 15,000×, 30,000×, and 60,000×) were obtained using a JEM-F200 (TFEG) (JEOL Ltd.) field-emission transmission electron microscope. The length of tau fibrils was measured using the ImageJ software. The fibril length was defined as the end-to-end distance of the identifiable negatively stained fibrils.

Tau-AC internalization by A549 cells

A549 cells (purchased from Korea Cell Line Bank; #10185) were cultured in RPMI media supplemented with 10% FBS, 2 mM L-glutamine, and 100 U/mL penicillin/streptomycin in a humidified atmosphere with 5% CO_2 at 37℃. To form tau-AC oligomers, recombinant tau-AC (100 μM) was incubated for 4 h at 37℃ on a rotating shaker. Next, oligomeric tau-AC (1 μM final concentration) was added to the cells. After 24 h, cells were trypsinized, re-plated into a new 24-

well plate, and allowed to adhere overnight. Immunofluorescence staining was performed to determine the localization of tau-AC aggregates.

Seeding of tau-AC aggregates into HEK293 tau-P301S FRET biosensor cells

Tau-RD-P301S-FRET cells (from ATCC #CRL-3275)[31] were cultured in a 24-well plate in DMEM media until cells reached ~70% confluency before transducing cells with tau-AC oligomers. The transduction complexes were generated by combining tau-AC (at the indicated concentration) with 5 µL of lipofectamine 2000 (Invitrogen) in opti-MEM (Glico) media for a final volume of 100 µL per well. The combined transduction complexes were incubated at room temperature (RT) for 15 min before being added to cells. After 24 h incubation, the effects of oligomeric tau-AC were analyzed by visualizing the cells using the GFP filter of the ECHO microscope.

Small-angle X-ray scattering (SAXS)

Solution SAXS experiments were performed at the 4C SAXS II beamline at the Pohang Accelerator Laboratory (Pohang, Republic of Korea). The concentration of tau-AC was adjusted to 1 mg/mL in a buffer solution (50 mM Tris-HCl, 6 M Gdn-HCl, pH 7.4), and the temperature was maintained at 20℃ during exposure to the X-ray beam. The sample-to-detector distance was set at 2 m. During each independent experiment, scattering patterns were recorded for 5 s and measured six times. The Guinier approximation of the SAXS profiles was performed to obtain the radius of gyration (R_g) (Equation 1), where q is the scattering vector, and $I(q)$ is the scattering intensity at q.

$$\ln[I(q)] = \ln[I(0)] - R_g^2/3q^2 \quad \text{(Equation 1)}$$

To demonstrate the unfolding of wild-type and phospho-mimetic tau-AC, a Kratky analysis of SAXS profiles ($I(q)\cdot q^2$ as a function of q) was performed. The dimensionless Kratky plot was obtained by multiplying the scattering vector q by R_g rather than q ($I(q)/I(0)\cdot(q\cdot R_g)^2$ as a function of $q\cdot R_g$). Modeling of representative structures for each tau-AC species was performed using EOM analysis from the ATSAS package.[49] External pools were used when running a genetic algorithm to optimize ensembles (GAJOE). The size of the ensemble was fixed at 50 curves per ensemble, and repetitions were disallowed. Each distribution was deconvoluted into three fractions with a gaussian distribution (R^2 values for fitting were 0.99759, 0.99141, 0.99186, and 0.99677 for tau-AC wt, S324D, S356D, and S324D/S356D, respectively).

CamSol analysis

For predicting the solubility of tau-AC at a pH = 7, we used the CamSol web server (http://www-vendruscolo.ch.cam.ac.uk/camsolmethod.html).[50]

Circular dichroism (CD) spectroscopy

CD spectroscopy analysis was performed to investigate the secondary structure of tau-AC wild type and mutant species in a monomeric form. For that purpose, 200 μL of 40 μM tau-AC sample was transferred to a quartz cuvette with a 1 mm path length. CD spectra were obtained from 200 to 250 nm at a scan speed of 20 nm/min five times using JASCO J-815 spectropolarimeter.

Electrospray Ionization (ESI) Mass Spectrometry (MS) combined with Ion Mobility Mass Spectrometry (IM-MS)

IM-MS was performed in positive ion mode using a Waters Synapt G2-Si HDMS quadrupole time-

of-flight (Q-TOF) mass spectrometer (Waters). The concentration of tau-AC samples was adjusted to 5 μM in 20 mM ammonium acetate (pH 6.8), and the proteins were transferred to the gas phase using an ESI source. The capillary voltage was 2.5 kV, and the source temperature was 80°C. The gas flow rates for the helium and drift cells were 180 and 90 mL/min, respectively, which provided a pressure of 3.23 mbar in the drift cell. The CCSs of the tau-AC conformers were calibrated following the procedure developed by Ruotolo *et al*.[51] and standards reported by Bush *et al*.[52]

Molecular Dynamics (MD) Simulations

The external pool (10,000 structures) generation was acquired from the replica-exchange MD (REMD) simulation with the CHARMM36m force field and the Generalized Born implicit solvation model using the GROMACS software package (version 4.5.5). The initial structure of the wild type tau-AC monomer was obtained from the tau fibril cryo-EM structure (PDB ID: 6VH7) from the Protein Data Bank (www.rcsb.org). Six replicas (T = 400, 419, 438, 459, 480, and 500 K) were used to obtain an average exchange probability of ~0.15. Each replica was simulated for 20 ns, and 10,000 MD-simulated random conformations were extracted from the replicas to perform EOM analysis. The simulation temperatures were generated by the 'remd-temperature-generator' web server (http://virtualchemistry.org/remd-temperature-generator/). MD simulations for dimeric forms were carried out using the GROMACS software package (version 2020.4) and supercomputing resources (KSC-2021-RND-0060) provided by the National Institute of Supercomputing and Network/Korea Institute of Science and Technology Information (KISTI). Based on the 30.4-μs REMD simulation (400 ns per replica) with the CHARMM36m force field, we calculated interchain contact probabilities of tau-AC homodimers. The initial structures were adopted from the replica-exchange Monte Carlo (REMC) simulations using the CAMPARI

simulation package (http://campari.sourceforge.net; ABSINTH model combined with the OPLS-AA/L parameters implemented in the abs3.2_opls.rpm parameter set). The most extended conformation based on R_g was selected and duplicated to form a dimer. The simulation protocol and data convergence analysis method were adapted from the protocol published by Man *et al*.[53] Simulations were performed at pH 7 in a cubic TIP3P water box containing 110 mM Na^+ and Cl^- ions. The GROMACS software package (version 2020.4) with the SHAKE algorithm allowed a time step of 2 fs. For electrostatic interactions, the particle mesh Ewald (PME) method with a cutoff of 1.2 nm was used, while for the van der Waals interactions, the cut-off was set to 1.2 nm, and a velocity-rescaling thermostat was employed. The REMD was carried out with 76 replicas from 300K to 400K, and exchanges between replicas were attempted every 2 ps with an exchange probability of 1.5. The RMSD from the initial structure was merged after 70 ns. The interchain distances between the β carbons of each side chain (α carbon for glycine) were calculated, and the residues were in contact if the distance between the two designated atoms was smaller than 0.8 nm. A Markov state model (MSM) analysis was performed using the TICAgg. We adopted interatomic distances between the carbon atoms to construct both inter- and intra-chain features. The number of dimensions was fixed at 10, and 300 k-means clustering centers were represented in the time-lagged independent component analysis (TICA) space and discretized into three groups. The structures in the figures were modelled using UCSF Chimera.

Primary rat cortical and hippocampal neurons

Primary neuron cultures were prepared from the rat embryonic cortex and hippocampus as previously reported.[54] Briefly, isolated cortical and hippocampal neurons were plated on poly-D-lysine-coated plates and coverslips, respectively, and incubated at 37°C in a humidified incubator

in Neurobasal medium (Invitrogen) supplemented with B-27 and L-glutamine (Invitrogen). At DIV 10, different concentrations of tau-AC aggregates were added to the media and cells were incubated for additional 3 days. At DIV 14, cells were lysed with 1% Triton X-100 buffer (50 mM Tris-HCl pH 8.0, 150 mM NaCl, 1% Triton X-100, 0.1% SDS, 2 mM EDTA, 1× PIC) for IB or fixed with 4% paraformaldehyde (PFA) for IF. To overexpress tau-AC and its phospho-mimetic mutants, they were first cloned into the FUGW lentiviral vector. Lentiviral particles were produced by co-transfection of vesicular stomatitis virus glycoprotein, Δ8.9, and the lentiviral vector in the packaging cell line HEK293T. After 60 h of incubation, the media containing the lentiviral particles was harvested, centrifuged to remove cellular debris, aliquoted, and stored at -80℃. Primary cultured neurons were infected with lentiviral particles expressing tau-AC and its mutants at DIV 6. At DIV 14, cells were lysed for IB or fixed for IF.

Chronic depolarization, polarized trafficking, and dendritic spines

At DIV 10, primary hippocampal neurons were transfected with EGFP, EGFP-tau-FL, and EGFP-tau-AC. After 48 h, the cultured neurons were depolarized by raising the KCl concentration of the medium from 5 mM to 15 mM for additional 48 h; 10 mM NaCl was added to the control cells. For IF, cells were fixed in 4% PFA in PBS for 20 min and then permeabilized with 0.25% Triton X-100 for 5 min. Next, sections were blocked for 1 h, incubated, first, with primary antibodies at 4℃ overnight, and, subsequently, with secondary antibodies for 3 h at RT with agitation. Fluorescent images were acquired using Zeiss LSM800 (40× lens, 512×512 pixels, and merging 0.4 μm Z-stacks by orthogonal projection) or ECHO Revolved Fluorescence microscope. The AIS length was measured and analyzed using the MATLAB Measurements and MathWorks program. The AIS start, maximum, and end positions were determined as previously described.[32] The data

for AIS positions were analyzed by two-way ANOVA with Turkey multiple comparison test. AIS length was defined as the length between the start and end points and data were analyzed using one-way ANOVA with Turkey multiple comparison tests. For polarized trafficking, plasmids expressing EGFP-tau-FL or EGFP-tau-AC were co-transfected with tdTOMATO (Addgene plasmid #51506) into DIV 13 hippocampal neurons for 24 h and AnkG immunostaining was performed as described above. The axon-to-dendrite ratio was calculated as [(axonal tau fluorescence/dendritic tau fluorescence)/(axonal area by tdTOMATO)/dendritic area by tdTOMATO].[55] The data were analyzed using Student's *t*-test and the GraphPad Prism 6 software. The area of the dendritic spine was measured by ImageJ plug-in SpineJ.[56] Dendrites were counted as tau-positive when EGFP-tau signals occupied more than 50% of tdTOMATO signals in total dendritic spine areas.

Stereotaxic injection

Stereotactic injections of tau-AC aggregates were performed using C57BL6/J wild-type mice (9-weeks-old, male). Mice were deeply anesthetized using intraperitoneal injection of a Zoletil/Rompun mixture (30 mg/kg and 10 mg/kg, respectively), fixed on a stereotaxic apparatus (Kopf instruments), and 1 μL of tau-AC aggregates (wt and S356D, 5 μg/μL) was unilaterally stereotaxically injected into the hippocampal CA1 region using a 30-gauge syringe (Hamilton). The coordinates were as follows: AP: -1.8 mm from the bregma, ML: +1.0 mm from the bregma, DV: -1.7 mm from the skull. The mock group underwent the same surgical procedures without the injection step. Experiments were conducted in accordance with the guidelines approved by the Institutional Animal Care and Use Committee of Seoul National University (IACUC #: SNU 171220-2-5).

Behavior tests

Open-field testing was used to measure the overall locomotor activity, novelty seeking, and anxiety levels of mice. In a white 32 cm × 32 cm × 40 cm arena, mice were placed at the center (20 cm × 20 cm) and tracked for 15 min using a computerized video tracking system. Anxiolytic and exploratory behaviors were characterized by exploring the center of the field rather than staying in the corner. Data were analyzed using the Ethovision 14 software (Noldus). Fear conditioning was performed as previously described with slight modifications.[57] Briefly, on day one, after exploring a fear conditioning chamber (Coulbourn Instruments) for 3 minutes, mice received three pairs of electrical footshocks (0.5 mA, 2 s) and a conditioned acoustic stimulus (CS, 80 dB, 2800 Hz, 30 s), which were co-terminated. The CS was delivered with 30 s-inter-tone interval. On day two, the mice were placed in the same fear conditioning chamber for 120 s. On the same day, the mice were place in a novel cylinder chamber and received the CS for 120 s after 120 s baseline period. During all sessions, freezing behavior for at least 1 s was automatically measured using the Freeze Frame software (ActiMetrics, IL, USA).

Perfusion

After anesthesia, mice were perfused with PBS, followed by 4% PFA. Brains were dissected, post-fixed in 4% PFA overnight at 4℃, and then transferred to a 30% (w/v) sucrose solution. Brains were sectioned into 30-μm coronal sections using a cryotome and stored in cryoprotectant solution (25% glycerol, 25% ethylene glycol, 20 mM phosphate buffer pH 7.4) at -20℃.

TUNEL assay

Apoptotic cells were identified using a TUNEL assay following the manufacturer's protocol (TUNEL Andy Fluor^{TM} 488 Apoptosis Detection Kit; ABP Biosciences) with minor modifications. Briefly, brain sections were washed twice in PBS, permeabilized with 0.2% Triton X-100/PBS for 30 min at RT, and then incubated in a TUNEL solution for 2 h in a humid chamber at 37℃. Next, samples were washed with 3% BSA in PBS and then placed in the staining solution for 1 h at RT.

Statistical analysis

Statistical significance of differences between various groups was determined by Student's t-test or one-way ANOVA followed by the Bonferroni *post hoc* test for most data. All experiments were performed in triplicated and data represent the mean standard deviation (SD). Differences were considered significant when *p*-values were less than 0.05.

COMPETING FINANCIAL INTERESTS

The authors declare no competing financial interests.

AUTHOR CONTRIBUTIONS

L.L. and J.L. carried out most of the biochemical experiments. D.I. and H.I.K. performed the biophysical analysis. S.P. and Y.H.S. conducted the AIS-related experiments. K.D.H. and Y.S.L. performed the mouse behavior analysis. Y.J. and J.H.L. prepared the recombinant proteins and primary neurons. M.J.L. Y.S.L., Y.H.S, H.I.K, and M.J.L. are responsible for the overall design of the study and manuscript preparation. All the authors reviewed the manuscript and approved the final version.

ACKNOWLEDGEMENTS

This work was supported by grants from the National Research Foundation of Korea (2021R1A2C2008023 to M.J.L., 2020R1A5A1019023 to Y.H.S., and M.J.L., 2021R1I1A1A01051245 to J.H.L., NRF-2018R1A5A2025964 to Y.-S.L., and 2019R1A2C2086193 to H.I.K.), the Korea Health Industry Development Institute and Korea Dementia Research Center (HU21C0071 to Y.H.S., H.I.K, and M.J.L.), and China Scholarship Council (CSC202108370145 to Y.J). This work was also supported by the National Institute of Supercomputing and Network (KSC-2021-RND-0060).

Note: All supplementary information and source data files are available in the online version of the paper.

REFERENCES

1. D. C. Chung, S. Roemer, L. Petrucelli and D. W. Dickson, *Mol Neurodegener*, 2021, **16**, 57.
2. A. Andreadis, *Prog Mol Subcell Biol*, 2006, **44**, 89-107.
3. J. H. Kim, J. Lee, W. H. Choi, S. Park, S. H. Park, J. H. Lee, S. M. Lim, J. Y. Mun, H. S. Cho, D. Han, Y. H. Suh and M. J. Lee, *Chem Sci*, 2021, **12**, 5599-5610.
4. F. A. Rojas Quijano, D. Morrow, B. M. Wise, F. L. Brancia and W. J. Goux, *Biochemistry*, 2006, **45**, 4638-4652.
5. A. W. P. Fitzpatrick, B. Falcon, S. He, A. G. Murzin, G. Murshudov, H. J. Garringer, R. A. Crowther, B. Ghetti, M. Goedert and S. H. W. Scheres, *Nature*, 2017, **547**, 185-190.
6. T. Arakhamia, C. E. Lee, Y. Carlomagno, D. M. Duong, S. R. Kundinger, K. Wang, D. Williams, M. DeTure, D. W. Dickson, C. N. Cook, N. T. Seyfried, L. Petrucelli and A. W. P. Fitzpatrick, *Cell*, 2020, **180**, 633-644 e612.
7. Y. Carlomagno, S. Manne, M. DeTure, M. Prudencio, Y. J. Zhang, R. Hanna Al-Shaikh, J. A. Dunmore, L. M. Daughrity, Y. Song, M. Castanedes-Casey, L. J. Lewis-Tuffin, K. A. Nicholson, Z. K. Wszolek, D. W. Dickson, A. W. P. Fitzpatrick, L. Petrucelli and C. N. Cook, *Cell Rep*, 2021, **34**, 108843.
8. C. Kontaxi, P. Piccardo and A. C. Gill, *Front Mol Biosci*, 2017, **4**, 56.
9. I. Grundke-Iqbal, K. Iqbal, Y. C. Tung, M. Quinlan, H. M. Wisniewski and L. I. Binder, *Proc Natl Acad Sci U S A*, 1986, **83**, 4913-4917.
10. A. D. Alonso, T. Zaidi, M. Novak, H. S. Barra, I. Grundke-Iqbal and K. Iqbal, *J Biol Chem*, 2001, **276**, 37967-37973.
11. S. Park, J. H. Lee, J. H. Jeon and M. J. Lee, *BMB Rep*, 2018, **51**, 265-273.
12. Y. Soeda and A. Takashima, *Front Mol Neurosci*, 2020, **13**, 590896.
13. T. J. Cohen, J. L. Guo, D. E. Hurtado, L. K. Kwong, I. P. Mills, J. Q. Trojanowski and V. M. Lee, *Nat Commun*, 2011, **2**, 252.
14. Y. Yan, X. Wang, D. Chaput, M. K. Shin, Y. Koh, L. Gan, A. A. Pieper, J. A. Woo and D. E. Kang, *Cell*, 2022, **185**, 3913-3930 e3919.
15. E. M. Mandelkow and E. Mandelkow, *Trends Cell Biol*, 1998, **8**, 425-427.
16. S. A. Kent, T. L. Spires-Jones and C. S. Durrant, *Acta Neuropathol*, 2020, **140**, 417-447.

17. X. Li, Y. Kumar, H. Zempel, E. M. Mandelkow, J. Biernat and E. Mandelkow, *EMBO J*, 2011, **30**, 4825-4837.
18. X. Sun, Y. Wu, M. Gu, Z. Liu, Y. Ma, J. Li and Y. Zhang, *Proc Natl Acad Sci U S A*, 2014, **111**, 14271-14276.
19. A. H. Song, D. Wang, G. Chen, Y. Li, J. Luo, S. Duan and M. M. Poo, *Cell*, 2009, **136**, 1148-1160.
20. S. L. Jones, F. Korobova and T. Svitkina, *J Cell Biol*, 2014, **205**, 67-81.
21. M. H. Kole, S. U. Ilschner, B. M. Kampa, S. R. Williams, P. C. Ruben and G. J. Stuart, *Nat Neurosci*, 2008, **11**, 178-186.
22. L. M. Palmer and G. J. Stuart, *J Neurosci*, 2006, **26**, 1854-1863.
23. C. Y. Huang and M. N. Rasband, *Ann N Y Acad Sci*, 2018, **1420**, 46-61.
24. B. R. Hoover, M. N. Reed, J. Su, R. D. Penrod, L. A. Kotilinek, M. K. Grant, R. Pitstick, G. A. Carlson, L. M. Lanier, L. L. Yuan, K. H. Ashe and D. Liao, *Neuron*, 2010, **68**, 1067-1081.
25. P. D. Sohn, C. T. Huang, R. Yan, L. Fan, T. E. Tracy, C. M. Camargo, K. M. Montgomery, T. Arhar, S. A. Mok, R. Freilich, J. Baik, M. He, S. Gong, E. D. Roberson, C. M. Karch, J. E. Gestwicki, K. Xu, K. S. Kosik and L. Gan, *Neuron*, 2019, **104**, 458-470 e455.
26. D. P. Hanger, B. H. Anderton and W. Noble, *Trends Mol Med*, 2009, **15**, 112-119.
27. C. Danis, E. Dupre, O. Zejneli, R. Caillierez, A. Arrial, S. Begard, J. Mortelecque, S. Eddarkaoui, A. Loyens, F. X. Cantrelle, X. Hanoulle, J. C. Rain, M. Colin, L. Buee and I. Landrieu, *Mol Ther*, 2022, **30**, 1484-1499.
28. D. A. Bateman and A. Chakrabartty, *Int J Alzheimers Dis*, 2011, **2011**, 962352.
29. C. S. Greil, I. M. Vorberg, A. E. Ward, K. D. Meade-White, D. A. Harris and S. A. Priola, *Virology*, 2008, **379**, 284-293.
30. P. H. Ren, J. E. Lauckner, I. Kachirskaia, J. E. Heuser, R. Melki and R. R. Kopito, *Nat Cell Biol*, 2009, **11**, 219-225.
31. B. B. Holmes, J. L. Furman, T. E. Mahan, T. R. Yamasaki, H. Mirbaha, W. C. Eades, L. Belaygorod, N. J. Cairns, D. M. Holtzman and M. I. Diamond, *Proc Natl Acad Sci U S A*, 2014, **111**, E4376-4385.
32. M. S. Grubb and J. Burrone, *Nature*, 2010, **465**, 1070-1074.

33. R. J. Hatch, Y. Wei, D. Xia and J. Gotz, *Acta Neuropathol*, 2017, **133**, 717-730.
34. S. F. Kazim, J. H. Seo, R. Bianchi, C. S. Larson, A. Sharma, R. K. S. Wong, K. Y. Gorbachev and A. C. Pereira, *eNeuro*, 2021, **8**.
35. A. Ittner and L. M. Ittner, *Neuron*, 2018, **99**, 13-27.
36. R. G. Phillips and J. E. LeDoux, *Behav Neurosci*, 1992, **106**, 274-285.
37. Y. Wang, S. Garg, E. M. Mandelkow and E. Mandelkow, *Biochem Soc Trans*, 2010, **38**, 955-961.
38. J. Gu, W. Xu, N. Jin, L. Li, Y. Zhou, D. Chu, C. X. Gong, K. Iqbal and F. Liu, *J Biol Chem*, 2020, **295**, 13812-13828.
39. E. Barini, G. Plotzky, Y. Mordashova, J. Hoppe, E. Rodriguez-Correa, S. Julier, F. LePrieult, I. Mairhofer, M. Mezler, S. Biesinger, M. Cik, M. W. Meinhardt, E. Ercan-Herbst, D. E. Ehrnhoefer, A. Striebinger, K. Bodie, C. Klein, L. Gasparini and K. Schlegel, *Neurobiol Aging*, 2022, **109**, 64-77.
40. H. H. Chen, P. Liu, P. Auger, S. H. Lee, O. Adolfsson, L. Rey-Bellet, J. Lafrance-Vanasse, B. A. Friedman, M. Pihlgren, A. Muhs, A. Pfeifer, J. Ernst, G. Ayalon, K. R. Wildsmith, T. G. Beach and M. P. van der Brug, *Sci Rep*, 2018, **8**, 16725.
41. T. Ishihara, M. Hong, B. Zhang, Y. Nakagawa, M. K. Lee, J. Q. Trojanowski and V. M. Lee, *Neuron*, 1999, **24**, 751-762.
42. F. Clavaguera, T. Bolmont, R. A. Crowther, D. Abramowski, S. Frank, A. Probst, G. Fraser, A. K. Stalder, M. Beibel, M. Staufenbiel, M. Jucker, M. Goedert and M. Tolnay, *Nat Cell Biol*, 2009, **11**, 909-913.
43. J. W. Vogel, Y. Iturria-Medina, O. T. Strandberg, R. Smith, E. Levitis, A. C. Evans, O. Hansson, I. Alzheimer's Disease Neuroimaging and S. Swedish BioFinder, *Nat Commun*, 2020, **11**, 2612.
44. M. Merezhko, R. L. Uronen and H. J. Huttunen, *Front Mol Neurosci*, 2020, **13**, 569818.
45. B. Frost, R. L. Jacks and M. I. Diamond, *J Biol Chem*, 2009, **284**, 12845-12852.
46. J. W. Wu, M. Herman, L. Liu, S. Simoes, C. M. Acker, H. Figueroa, J. I. Steinberg, M. Margittai, R. Kayed, C. Zurzolo, G. Di Paolo and K. E. Duff, *J Biol Chem*, 2013, **288**, 1856-1870.
47. B. B. Holmes, S. L. DeVos, N. Kfoury, M. Li, R. Jacks, K. Yanamandra, M. O. Ouidja, F.

M. Brodsky, J. Marasa, D. P. Bagchi, P. T. Kotzbauer, T. M. Miller, D. Papy-Garcia and M. I. Diamond, *Proc Natl Acad Sci U S A*, 2013, **110**, E3138-3147.

48. G. Xu, V. Gonzales and D. R. Borchelt, *Alzheimer Dis Assoc Disord*, 2002, **16**, 191-195.
49. G. Tria, H. D. Mertens, M. Kachala and D. I. Svergun, *IUCrJ*, 2015, **2**, 207-217.
50. P. Sormanni, F. A. Aprile and M. Vendruscolo, *J Mol Biol*, 2015, **427**, 478-490.
51. B. T. Ruotolo, J. L. Benesch, A. M. Sandercock, S. J. Hyung and C. V. Robinson, *Nat Protoc*, 2008, **3**, 1139-1152.
52. M. F. Bush, Z. Hall, K. Giles, J. Hoyes, C. V. Robinson and B. T. Ruotolo, *Anal Chem*, 2010, **82**, 9557-9565.
53. V. H. Man, P. H. Nguyen and P. Derreumaux, *J Phys Chem B*, 2017, **121**, 5977-5987.
54. J. M. Song, M. Kang, D. H. Park, S. Park, S. Lee and Y. H. Suh, *J Neurosci*, 2021, **41**, 2344-2359.
55. J. F. Rivera, S. Ahmad, M. W. Quick, E. R. Liman and D. B. Arnold, *Nat Neurosci*, 2003, **6**, 243-250.
56. F. Levet, J. Tønnesen, U. V. Nägerl and J.-B. Sibarita, *Methods*, 2020, **174**, 49-55.
57. J. H. Kim, A. Kim, Y. Yun, S. Park, J. H. Lee, Y. S. Lee and M. J. Lee, *Mol Brain*, 2020, **13**, 4.

FIGURE LEGENDS

Figure 1. *In vitro* self-aggregating and seeding properties of the tau aggregation core of Alzheimer's disease (tau-AC). (**A**) Schematic diagram depicting the domains of full-length tau (tau-FL), tau-AC (residues 306–378), and locations of each antibody epitope. (**B**) The evaluation of tau-AC self-aggregation propensity in the absence of inducers. The FLAG-tagged recombinant tau-AC (100 μM) was incubated at 37℃ with mild agitation (250 rpm) for indicated time periods and then analyzed using non-reducing SDS-PAGE followed by immunoblotting (IB) against FLAG antibodies (*left*) and Coomassie Brilliant Blue (CBB) staining (*right*). (**C**) Seeding ability of tau-AC. Recombinant tau-FL (20 μM) was incubated alone or with tau-AC (20 μM) at 37℃ with agitation for indicated time periods. Induction of tau-FL aggregation by tau-AC was evaluated by IB using TAU-5 antibodies and CBB staining (*left*). Self-aggregation of tau-AC was detected using FLAG and TAU-AC antibodies (*right*). (**D**) Tau-FL (20 μM) was incubated with either heparin (80 μM) or tau-AC (20 μM) for 4 days. The samples were loaded and filtered into each well of a 96-well plate under either reducing or non-reducing conditions. The trapped tau oligomers loaded onto the cellulose acetate membrane were detected by IB using TAU-5 (for tau-FL) and TAU-AC antibodies. (**E**) The samples (4 μM) from the fibrillization reactions performed as described in (C) were incubated with thioflavin T (50 μM), and fluorescence intensity at 485 nm was measured. Error bars represent standard errors of the mean. RFU, relative fluorescence unit. $*p < 0.05$, $**p < 0.01$, $***p < 0.001$ (n = 3, one-way ANOVA). (**F**) Representative images of negatively stained tau filaments observed by transmission electron microscopy (TEM). Tau-FL (20 μM) and tau-AC (20 μM) were incubated for 2 days at 37℃. White and blue scale bars represent 500 nm and 200 nm, respectively. (**G**) Quantification of data presented in (**F**). The length

and width of tau filaments were plotted as the mean ± SD. ***$p < 0.001$ (n = 100/group, one-way ANOVA). (**H**) Tubulin monomers (4 mg/mL) were polymerized in the presence of tau-FL or tau-AC (10/1 molar ratio of tubulin/tau) in a GTP-containing buffer at 37°C. Microtubule assembly was kinetically monitored by the fluorescence signal from DAPI incorporation into the microtubules (excitation/emission at 358/461 nm). (**I**) After the microtubule polymerization reaction, the samples were fractionated by ultracentrifugation at 68,000× *g* for 20 min. Supernatants (S) and pellets (P) were subjected to SDS-PAGE and analyzed by CBB staining and IB analysis with indicated antibodies.

Figure 2. Biochemical and biophysical analysis for mechanistic evaluation of tau-AC self-aggregation. (**A**) Serines at 324 and 356 positions of tau-AC were mutated to aspartic acids to mimic its phosphorylation (tau-AC-S324D, -S356D, and -S324D/S356D [SDSD] mutants; *top*). Wild-type tau-AC (tau-AC-wt) or phospho-mimetic mutants (phospho-tau-AC; 40 μM each) were incubated at 37°C for indicated time periods. Samples were subjected to non-reducing SDS-PAGE/IB (*bottom*). (**B**) The conversion of tau-AC into insoluble aggregates was analyzed by filter trap assays over a 3-day period. Trapped tau fibrils were detected by IB using TAU-AC antibodies (*top*), quantified, and plotted as the mean ± SD (*bottom*); results from three independent experiments. (**C**) Phospho-tau-AC lacks the seeding ability. Tau-FL (20 μM) was incubated with tau-AC or phospho-tau-AC (20 μM) at 37°C for 24 h, and the assembly reactions were ultracentrifuged at 120,000× *g* for 1 h to obtain the supernatant and pellet fractions. The fractions, as well as whole cell lysates, were analyzed by SDS-PAGE/IB using TAU-5 (for tau-FL) and FLAG (for tau-AC) antibodies. (**D**) The radius of gyration (R_g) values and R_g distribution of tau-AC-wt and tau-AC-S324D, -S356D, and -SDSD mutants were obtained from Guinier analysis of

the small-angle X-ray scattering (SAXS) profiles. The error bars represent the standard deviation of two independent SAXS experiments. (**E**) Raw X-ray scattering patterns with experimental SAXS profiles (black dots) and the fitted curves (red lines) obtained from the ensemble optimization method (EOM) from tau-AC-wt and three phospho-mimetic mutants. (**F**) Deconvoluted R_g distribution from the EOM analysis and the representative structures of each tau-AC species. (**G**) Collision cross-section (CCS) distribution of tau-AC-wt and the mutants. (**H**) Interchain contact probability maps of tau-AC-wt and -SDSD mutant from 30.4 μs molecular dynamics simulation trajectory. Red boxes indicate the ^{306}VQIVYK^{311} hexapeptides located at the N-termini of tau-AC. (**I**) Decreased levels of phospho-S356-tau were detected from whole-brain lysates of 15-month-old AD model mice overexpressing mutant amyloid precursor protein and presenilin-1 (APP/PS1), compared to those of wild-type littermate controls (N = 3 per group).

Figure 3. Cellular uptake of tau-AC aggregates by cultured cells and primary neurons. (**A**) (*left*) Representative confocal images of A549 cells after treatment with monomeric and oligomeric forms of tau-AC^{FLAG} (1 μM) for 24 h. Cells were trypsinized, re-plated onto the new glass coverslips, and then stained with anti-FLAG and anti-α-tubulin antibodies. Internalized tau-AC aggregates were imaged as Z-stacks (X-Z and Y-Z cross sections). (*right*) The percentage of tau-AC-positive cells in the whole population and the number of tau-AC aggregates per cell were quantified and presented as the mean ± SD of three independent experiments. ***$p < 0.001$ (n > 100 cells per group, two-tailed Student's *t*-test). (**B**) A549 cells were pre-treated for 1 h with endocytosis inhibitors genistein (200 μM), chlorpromazine (20 μM), and amiloride (500 μM), incubated with oligomeric tau-AC for 24 h, and then the percentage of tau-AC-positive cells and the number of aggregates per cell were quantified. *$p < 0.01$ (n > 100 cells per group, one-way

ANOVA). n.s., not significant. (**C**) Förster resonance energy transfer (FRET)-based analysis of tau-AC seeding effects in HEK293 tau-P301S biosensor cells. The cells were treated with 1 μM of tau-AC monomers and oligomers for 24 h, and a relative FRET-positive cell number was quantified. Data represent the mean ± SD. ***$p < 0.001$ (n > 500 cells/group, two-tailed Student's *t*-test). (**D**) HA-tagged tau-AC was fused with NS3 protease containing an auto-cleavage site located between NS3 and tau-AC. HEK293T cells were co-transfected with plasmids expressing NS3-tau-AC and tau-FL for 30 h and then treated with MG132 (10 μM) for additional 6 h. Cells were lysed in RIPA buffer, whole cell lysates (WCLs) were separated into RIPA-soluble (supernatant) and -insoluble (pellet) fractions and subjected to non-reducing (supernatants) and reducing (pellets) SDS-PAGE/IB. (**E**) Primary cortical rat neurons were infected with lentiviruses expressing Myc-tagged tau-AC and its phospho-mimetic mutants on the *in vitro* day 6 (DIV 6). Whole neuron lysates were collected on DIV 13 and subjected to SDS-PAGE/IB.

Figure 4. Impaired AIS plasticity in primary hippocampal neurons overexpressing tau-AC. (**A**) Shortened AIS lengths with tau-AC during chronic depolarization. EGFP-tagged tau-FL and tau-AC were transiently overexpressed in DIV 10 primary hippocampal neurons. On DIV 12, the infected neurons were further treated with either 15 mM of NaCl (as controls) or KCl (for depolarization) for another 48 h. Representative confocal images (*top*) and quantification of AIS localization and lengths (*bottom*) are shown. The start and end points of the AIS detected by ankyrin G (AnkG) immunostaining are indicated with white arrowheads. Distances along axon and AIS lengths were analyzed by one-way ANOVA with Tukey multiple comparison test. The number of neurons used for each quantification is displayed at the bottom of the graph. Scale bar, 10 μm. (**B**) βIV-spectrin and EB3 immunostaining of the EGFP-tau-FL or EGFP-tau-AC-infected

neurons (*left*) and quantification of AIS lengths (*right*) using the unpaired Student's *t*-test. The boundary of soma is shown with a white dashed line. Scale bar, 10 μm. (**C**) Polarized trafficking is affected in neurons overexpressing tau-AC. DIV 14 hippocampal neurons were co-transfected with EGFP-tau-FL or -AC and tdTOMATO. After 24 h, cells were immunostained with anti-AnkG antibody and Z-stacked confocal microscopy images were acquired. Using MetaMorph software, axonal and dendritic tau signals were quantified using AnkG-positive axon and soma-excluded dendritic branches, respectively. Axon to dendritic tdTOMATO signal intensities were obtained in the same manner and used to normalize the results. Arrowheads indicate AnkG-positive axons. ***$p < 0.001$ (unpaired Student's t-test). Scale bar, 25 μm. (**D**) Effect of tau-AC on dendritic spine density and tau localization in primary rat neurons. EGFP-tau-FL and -AC were overexpressed in DIV 13 neurons, and fluorescence signals were obtained using Z-stacked confocal microscopy on DIV 21. Representative images and spine quantification are shown. Tau-positive spines were determined using the semi-automated NeuronJ program. Bars represent the percentage of tau-positive dendritic spines and the number of total spines (mean ± SD; unpaired Student's t-test). Scale bar, 5 μm.

Figure 5. Evaluation of behavioral and biochemical phenotypes in mice after hippocampal injection of tau-AC aggregates. (**A**) Experimental design of the study. A unilateral injection of either tau-AC-wt or -S356D mutant aggregates (5 μg tau-AC/1 μL saline) was administered into the hippocampus of wild-type mice (9 weeks old). The sham-operated control group underwent the same surgical procedures without the injection step. Hip, hippocampus; Th, thalamus. (**B**) Coronal sections were co-immunostained with anti-NeuN and FLAG antibodies for neuron and tau-AC, respectively. Nuclei were counterstained with DAPI. The ipsilateral hippocampal regions

two months after tau-AC injection are shown. CA1, cornu ammonis 1; DG, dentate gyrus. (**C**) Representative images of tau-AC signal in the CA1 area of the ipsilateral hippocampus. Magnified views of boxed areas are shown on right. (**D**) Apoptotic neurons in the hippocampus were visualized by the terminal deoxynucleotidyl transferase dUTP nick-end labeling (TUNEL) assay. (**E**) Immunostaining of GFAP, a glial marker. High intensity GFAP staining in the CA1 layer is primarily overlapped with the NeuN-positive signal in mice injected with tau-AC-wt, and to a lesser degree with tau-AC-S356D. White scale bars = 400 μm, red scale bars = 150 μm. (**F**) One month after stereotaxic injection, mice were subjected to the open-field test, and their general locomotive activity and anxiety-like behavior were measured. Representative trace images of the open-field test (*left*), where a center zone is indicated with a white box. Quantification of moving distances (*middle*) and times in the central region (*right*) is shown. Data were analyzed using one-way ANOVA (mock, n = 9; tau-AC-wt, n = 9; tau-AC-S356D, n = 10) and presented as the mean ± SEM. (**G**) Freezing behaviors during conditioning, contextual memory retrieval, and tone memory retrieval tasks were evaluated. Two months after tau-AC injection, mice were trained using three pairs of acoustic tones and electric foot shocks. Freezing behavior at the baseline and in response to tones and inter-tone intervals was monitored (*left*). The next day, freezing behavior was measured in the same conditioning chamber to test contextual fear memory (*middle*). An auditory fear memory was examined in a novel context by measuring freezing at the baseline and in response to tones (*right*). Samples were analyzed using one-way ANOVA with Tukey post-hoc test (mock, n = 9; tau-AC-wt, n = 9; tau-AC-S356D, n = 10).

Figure 6. The proposed model of tau-AC-induced pathogenesis. Tau-AC has a weaker binding affinity to microtubules than tau-FL and, during the onset of tauopathies, free (unbound) tau-AC

species spontaneously oligomerize through its N-terminal residues forming proto-filaments. Neurons can internalize the oligomeric forms of tau-AC through endocytosis, which subsequently leads to endogenous tau aggregation. However, phospho-mimetic tau-AC exhibits a drastically reduced aggregation propensity, suggesting that this phosphorylation may have anti-amyloidogenic properties. The pathologic tau species are mislocalized in somatodendrites and dendritic spines due to the perturbed AIS function, ultimately causing excitotoxicity. The clinical significance of this tau fragment in various tauopathies remains to be determined. However, these findings may pave the way for the development of novel pharmacological methods that would inhibit tau filament formation.

SUPPLEMENTARY FIGURE LEGENDS

Figure S1. Seeding effect of tau-AC on tau-FL aggregation *in vitro*. (**A**) Tau-FL (20 μM) and tau-AC^{FLAG} (20 μM) were incubated at 37℃ with mild agitation. After 3 days, samples were subjected to non-reducing SDS-PAGE and immunoblotting (IB) using anti-FLAG, TAU-5, and TAU-AC antibodies. (**B**) Samples were incubated as described in (A) with various reactant ratios and incubation times as indicated. (**C**) Tau-FL was incubated with tau-AC (molar ratios 0.1, 0.5, or 1.0) for 2 days, and thioflavin T fluorescence intensity was measured at 485 nm. (**D**) Tau-FL (20 μM) proteins were incubated with either heparin (80 μM) or tau-AC (20 μM) for 4 days and then subjected to ultracentrifugation at 120,000× *g* for 1 h. The supernatant and pellet fractions were collected and analyzed by SDS-PAGE/IB with antibodies as indicated. These data supplement Figure 1.

Figure S2. Biochemical and biophysical analysis of tau-AC and its phospho-mimetics. (**A**) *In vitro* phosphorylation reactions were performed by incubating tau-AC and GSK3β at 30℃ for 16 h. Next, phosphorylated tau-AC (20 μM) was incubated with tau-FL (20 μM) for 2 days at 37℃ with mild agitation and samples were analyzed by IB using antibodies as indicated. (**B**) Kratky analysis of tau-AC wild-type (wt), its single phospho-mimetic mutants (S324D and S356D), and double phospho-mimetic mutants (S324D/S356D) based on small-angle X-ray scattering profiles. (**C**) Circular dichroism spectra of tau-AC-wt and phospho-mimetic mutants. (**D**) CamSol solubility profile of tau-AC at neutral pH (pH = 7). The PHF6 residues (amino acids 306 – 311) located at the N-terminus exhibits poor solubility. (**E**) The collision cross-section calibration curves using standard proteins with known CCS values, such as ubiquitin, cytochrome C, and apomyoglobin

$R^2 > 0.999$). (**F**) Root-mean-square deviation (RMSD) data from the MD simulation (*top*) and the representative structures (*bottom*) of tau-AC-wt homodimers. The RMSD from the initial structure became merged after 70 ns. Two chains in the structure are depicted in different colors (orange and green) and the C-terminal end of each chain is presented as a sphere. These data supplement Figure 2.

Figure S3. Reduced aggregation propensity of tau-AC mutants lacking the N-terminal PHF6 motif. (**A**) Schematic diagram of tau-AC mutants where the PHF6 motif was deleted (tau-AC-ΔPHF6) or substituted with hydrophilic residues (tau-AC-TQDVSK), and the C-terminal tau fragment from the R1 domain to the C-terminus (tau-ΔN). (**B** and **C**) Markedly reduced self-aggregation (B) and ThT signals (C) of the mutants and comparison with tau-AC. The identical experiments were performed as in Fig. 1B and Fig. 1E, respectively, except that the tau-AC mutants were used. (**D**) Loss of seeding ability of tau-AC mutants lacking the PHF6 motif. (**E**) ThT assay using tau-AC-wt or mutants along with tau-FL. (**F**) Direct interaction between end-binding protein 3 (EB3) and tau-AC. Using lentiviral infection, FLAG-tagged EB3 and EGFP-tagged tau-FL, tau-AC, or tau-ΔR1234 (the mutant with four repeats of microtubule-binding domains being deleted) were transiently overexpressed in primary cortical neurons for 2 days. Whole-cell lysates were subjected to immunoprecipitation using anti-GFP antibodies, followed by IB as indicated. L.C., light chain; H.C., heavy chain.

Figure S4. Internalization of tau-AC aggregates into cells. (**A**) Day 10 *in vitro* (DIV 10) primary rat hippocampal neurons were treated with oligomerized tau-AC (0.1 μM) for 3 days, vigorously washed three times, and then co-immunostained using anti-MAP2 (for differentiated neuron) and

anti-FLAG (for tau-AC) antibodies. Nuclei were counterstained with DAPI. Yellow arrows indicate intraneuronal tau-AC. (**B**) Primary neurons were cultured as described in (A) but cells were co-stained for different neuronal markers β-tubulin III/Tuj-1. (**C**) A549 cells were treated with 1 μM of tau-AC aggregates for 24 h, trypsinized, replated, and then immunostained with anti-FLAG (tau-AC) anti-Rab5 (early endosomes), anti-Rab7 (late endosomes), or anti-LAMP1 (lysosomes) antibodies. Arrowheads point to tau-AC colocalized with the components of the endosome-lysosomal pathway. (**D**) HEK293 tau-P301S biosensor cells were treated with oligomeric forms of tau-AC-wt. After 24 h, FRET signals were measured on fixed cells. FRET-positive signals were not observed in cells treated with tau-AC monomers. (**E**) As in (D), except that 1 μM of tau-AC-wt and its phospho-mimetic mutants (tau-AC-S324D, -S356D-, and -SDSD) were used to obtain the FRET images. (**F**) Representative images of A549 cells incubated with tau-AC-wt and its phospho-mimetic mutants for 24 h. Internalized tau-AC species were detected by immunofluorescence using an anti-FLAG antibody. These data supplement Figure 3.

Figure S5. The effect of stereotaxically injected tau-AC-wt or -S356D on the behavioral and biochemical phenotypes of mice. (**A**) Experimental design. (**B**) Quantitation of Figure 5B. Intensities of FLAG-positive signals (tau-AC) were measured and plotted as mean ± SD (mock, n = 9; tau-AC-wt, n = 9; tau-AC-S356D, n = 10). *$p < 0.05$, **$p < 0.01$, ***$p < 0.001$ (one-way ANOVA followed by the Bonferroni post hoc test). (**C** and **D**) Two months after the ipsilateral injection of tau-AC-wt or tau-S356D, the mice were sacrificed and neurofibrillary tangles in the CA1 region were detected in the coronal sections of the brains using anti-AT-8 (C) and anti-T22 (D) antibodies. (**E**) Neurofibrillary tangles in the hippocampus areas (*upper*) and CA1 regions

(*lower*) were detected using thioflavin S staining. White scale bars = 400 μm; red scale bars = 150 μm. Thioflavin intensities were measured and plotted as mean ± SD of three independent slides (one-way ANOVA followed by the Bonferroni post hoc test). (**F**) The dendrite gyrus (DG) and CA2-CA3 regions were stained for NeuN (neuron marker) and FLAG (injected tau-AC). (**G**) Experiments were performed as described in Fig. 5B; lower magnifications with the contralateral sides are shown. Hip, hippocampus (green arrowheads); Th, thalamus. Yellow arrowheads indicate the CA1 regions with neurotoxicity, which correspond to tau-AC signal colocalization.

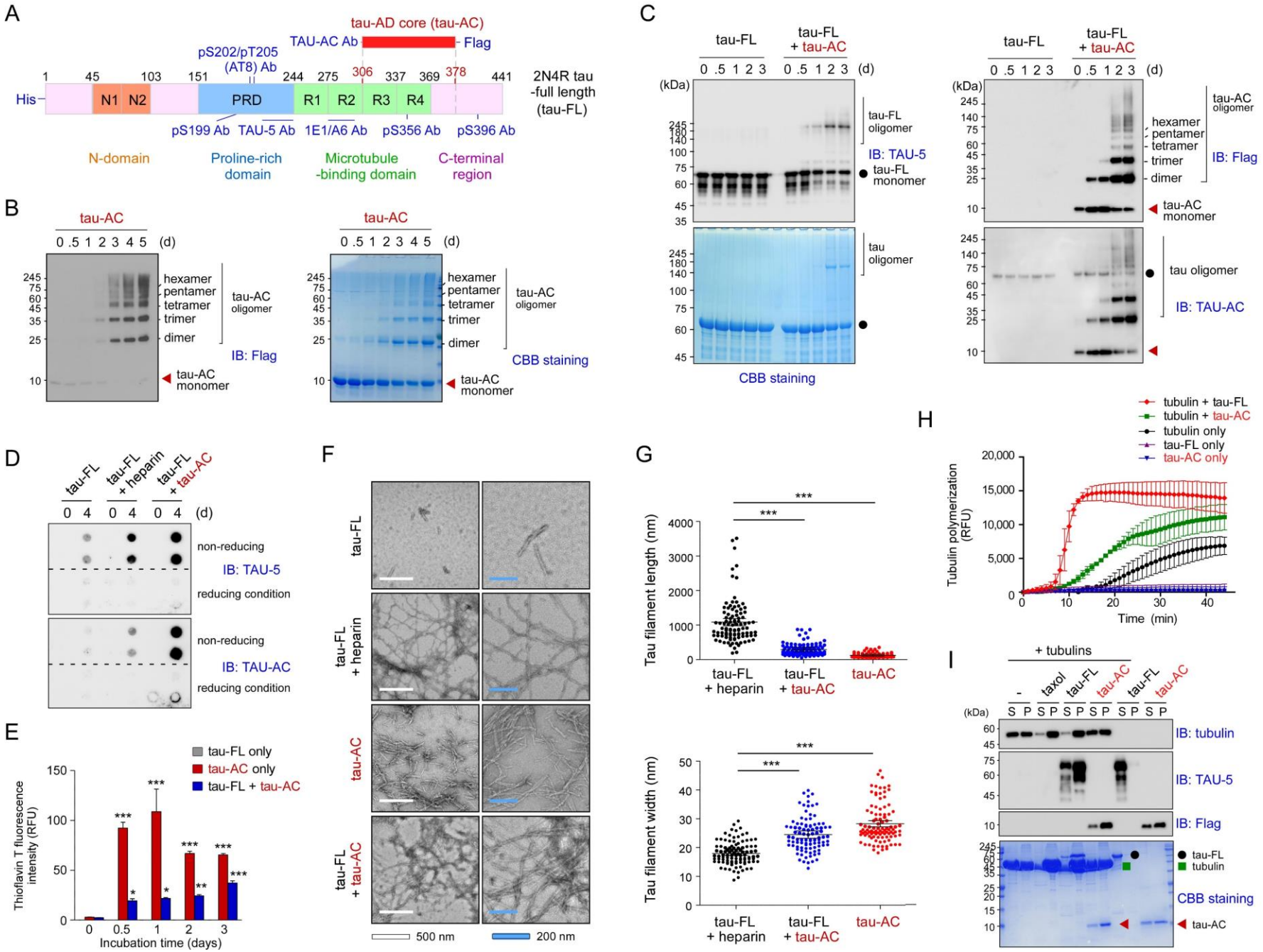
A
tau-AD core (tau-AC)
TAU-AC Ab
Flag
pS202/pT205 (AT8) Ab
His
N1
N2
PRD
R1
R2
R3
R4
2N4R tau -full length (tau-FL)
pS199 Ab
TAU-5 Ab
1E1/A6 Ab
pS356 Ab
pS396 Ab
N-domain
Proline-rich domain
Microtubule -binding domain
C-terminal region
B
tau-AC
hexamer
pentamer
tetramer
trimer
dimer
tau-AC oligomer
IB: Flag
tau-AC monomer
CBB staining
C
tau-FL
tau-FL + tau-AC
tau-FL oligomer
IB: TAU-5
tau-FL monomer
tau oligomer
CBB staining
tau-AC oligomer
IB: Flag
tau-AC monomer
tau oligomer
IB: TAU-AC
D
tau-FL
tau-FL + heparin
tau-FL + tau-AC
non-reducing
IB: TAU-5
reducing condition
IB: TAU-AC
E
tau-FL only
tau-AC only
tau-FL + tau-AC
Thioflavin T fluorescence intensity (RFU)
Incubation time (days)
F
tau-FL
tau-FL + heparin
tau-AC
tau-FL + tau-AC
500 nm
200 nm
G
Tau filament length (nm)
Tau filament width (nm)
tau-FL + heparin
tau-FL + tau-AC
tau-AC
H
tubulin + tau-FL
tubulin + tau-AC
tubulin only
tau-FL only
tau-AC only
Tubulin polymerization (RFU)
Time (min)
I
+ tubulins
taxol
IB: tubulin
IB: TAU-5
IB: Flag
tau-FL
tubulin
CBB staining
tau-AC

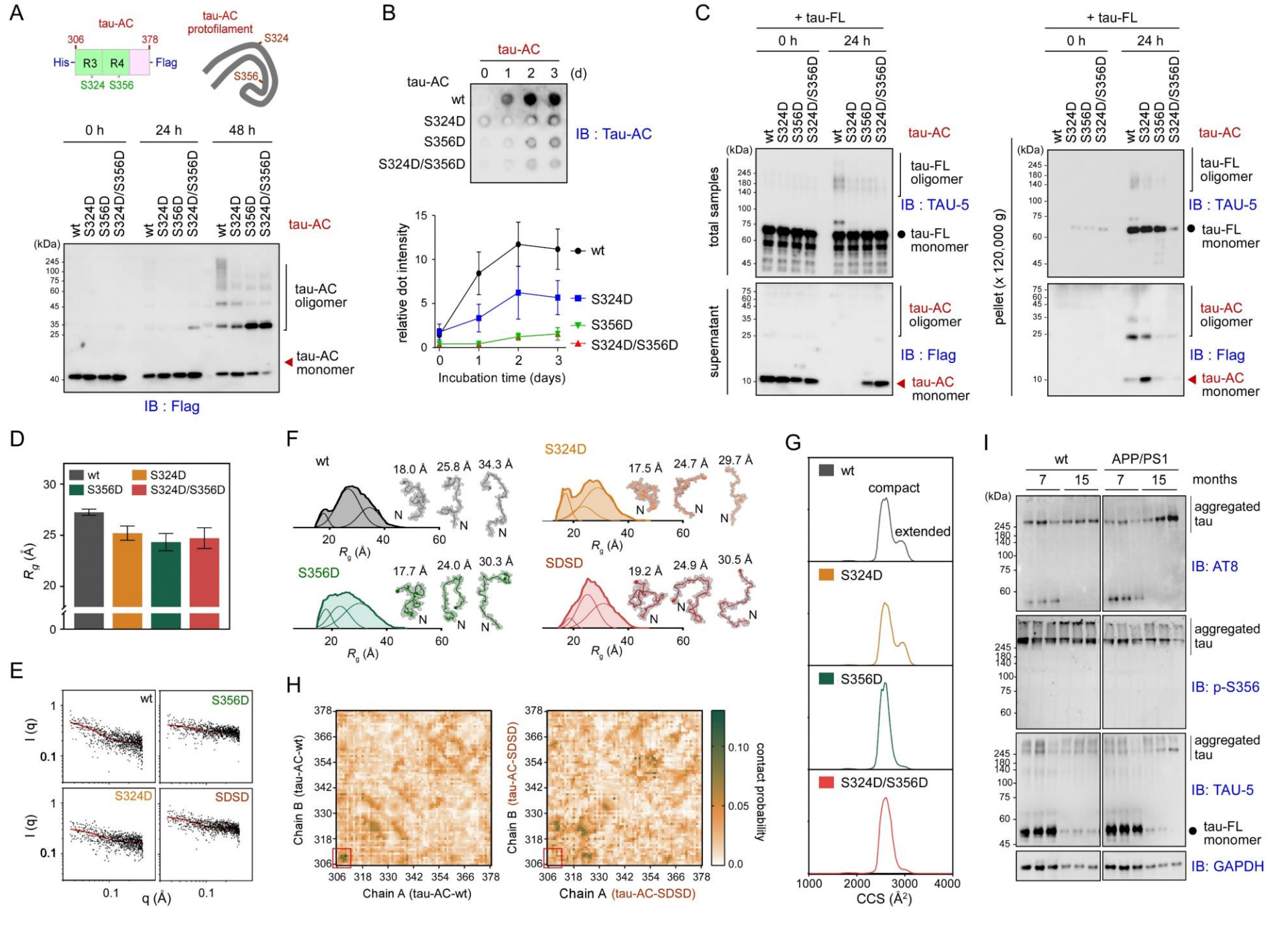
A
tau-AC
306
378
His
R3
R4
Flag
S324
S356
tau-AC protofilament
S324
S356
0 h
24 h
48 h
wt
S324D
S356D
S324D/S356D
tau-AC
(kDa)
tau-AC oligomer
tau-AC monomer
IB : Flag
B
tau-AC
0 1 2 3 (d)
wt
S324D
S356D
S324D/S356D
IB : Tau-AC
relative dot intensity
Incubation time (days)
C
+ tau-FL
0 h
24 h
total samples
supernatant
pellet (x 120,000 g)
tau-FL oligomer
tau-FL monomer
tau-AC oligomer
tau-AC monomer
IB : TAU-5
IB : Flag
D
wt
S324D
S356D
S324D/S356D
R_g (Å)
E
wt
S356D
S324D
SDSD
I (q)
q (Å)
F
wt
S324D
S356D
SDSD
R_g (Å)
G
wt
compact
extended
S324D
S356D
S324D/S356D
CCS (Å²)
H
Chain B (tau-AC-wt)
Chain A (tau-AC-wt)
Chain B (tau-AC-SDSD)
Chain A (tau-AC-SDSD)
contact probability
I
wt
APP/PS1
7
15
months
aggregated tau
IB: AT8
IB: p-S356
IB: TAU-5
IB: GAPDH
tau-FL monomer

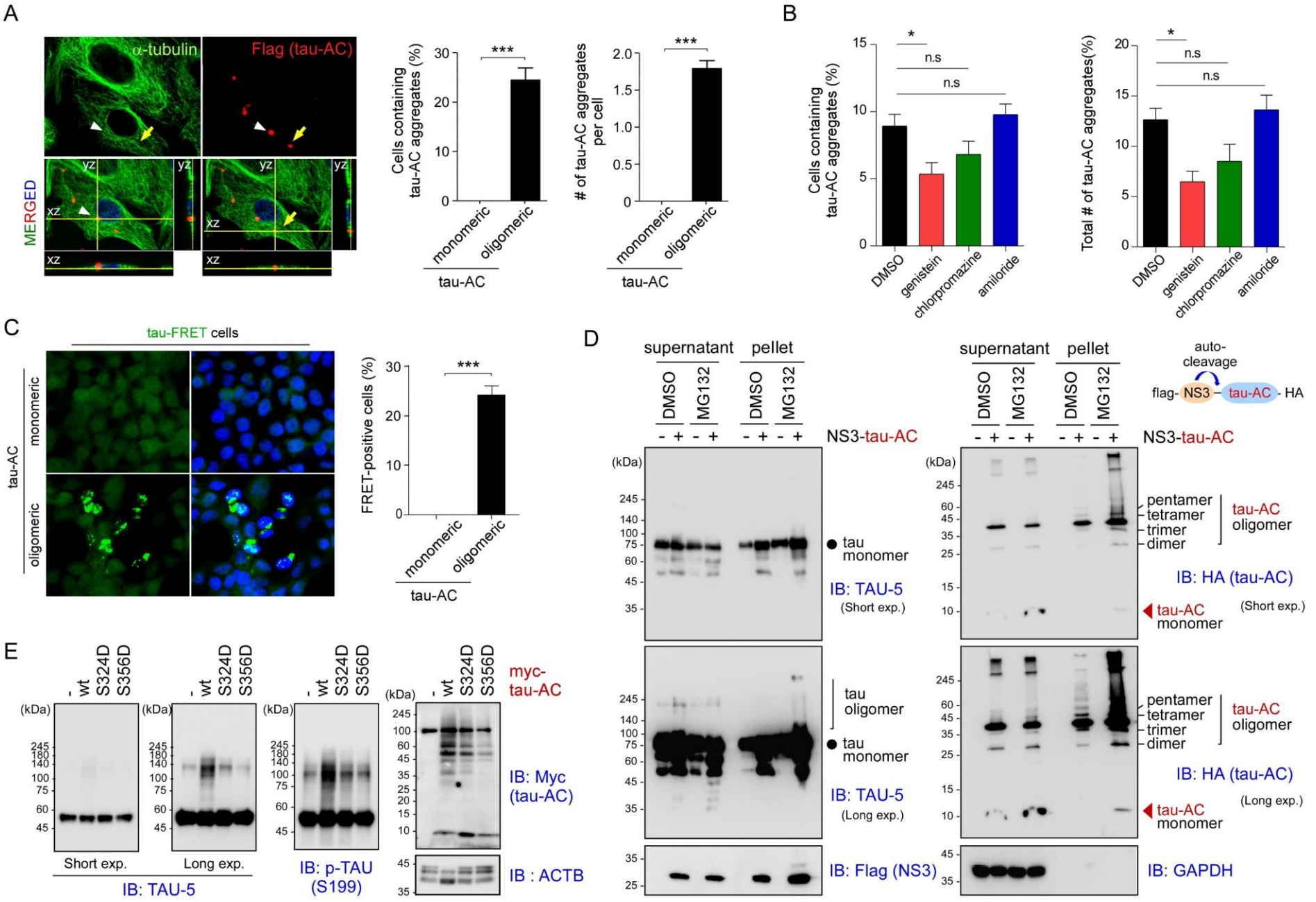
A
α-tubulin
Flag (tau-AC)
MERGED
yz
xz
Cells containing tau-AC aggregates (%)
***
monomeric
oligomeric
tau-AC
# of tau-AC aggregates per cell
B
Cells containing tau-AC aggregates (%)
Total # of tau-AC aggregates(%)
*
n.s
DMSO
genistein
chlorpromazine
amiloride
C
tau-FRET cells
tau-AC
monomeric
oligomeric
FRET-positive cells (%)
D
supernatant
pellet
DMSO
MG132
NS3-tau-AC
(kDa)
tau monomer
IB: TAU-5
(Short exp.)
tau oligomer
(Long exp.)
auto-cleavage
flag- NS3 – tau-AC - HA
pentamer
tetramer
trimer
dimer
tau-AC oligomer
IB: HA (tau-AC)
tau-AC monomer
IB: Flag (NS3)
IB: GAPDH
E
- wt S324D S356D
myc-tau-AC
Short exp.
Long exp.
IB: TAU-5
IB: p-TAU (S199)
IB: Myc (tau-AC)
IB : ACTB

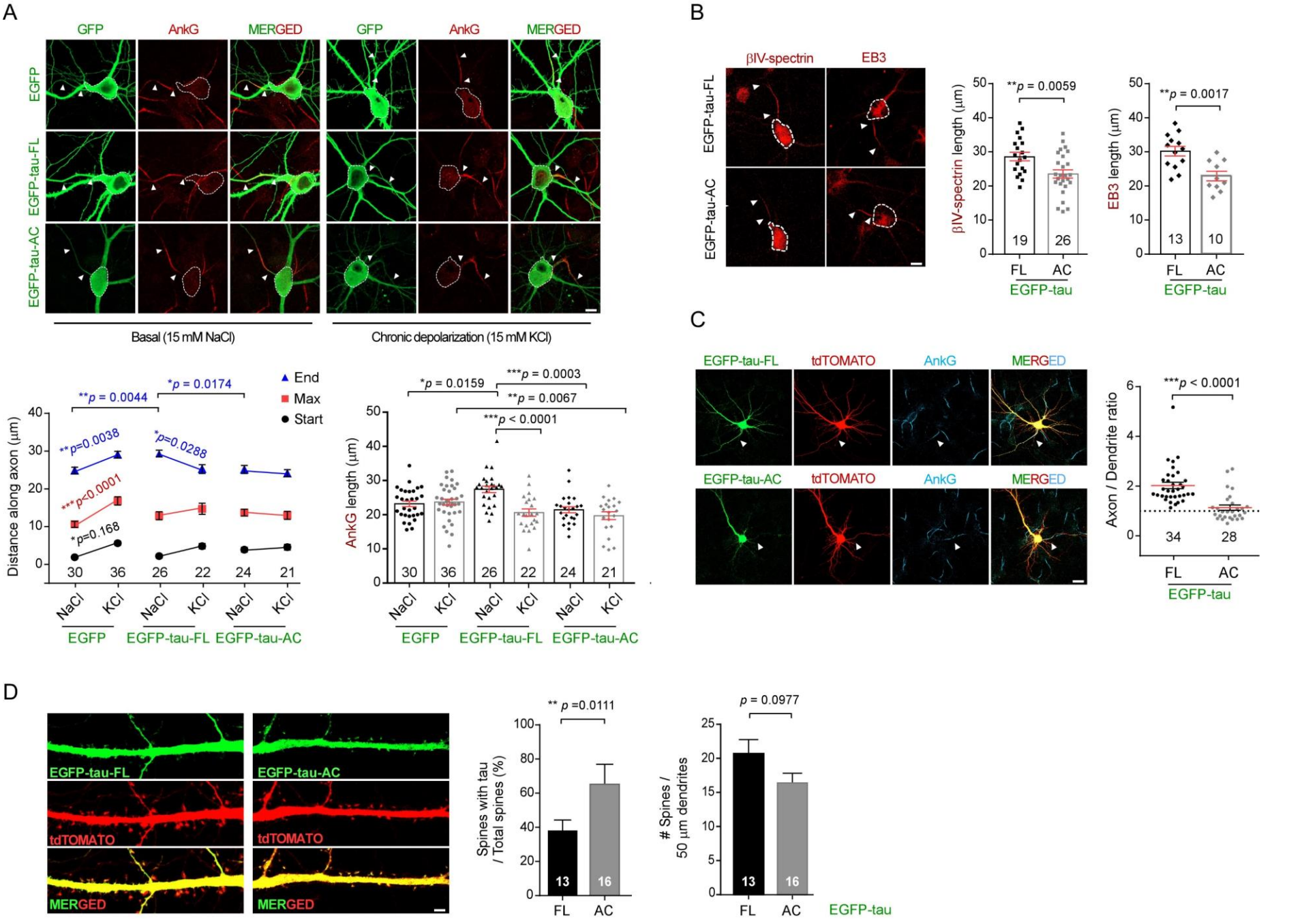
A
GFP
AnkG
MERGED
EGFP
EGFP-tau-FL
EGFP-tau-AC
Basal (15 mM NaCl)
Chronic depolarization (15 mM KCl)
End
Max
Start
Distance along axon (µm)
**p = 0.0044
*p = 0.0174
**p=0.0038
*p=0.0288
***p<0.0001
*p=0.168
30
36
26
22
24
21
NaCl
KCl
EGFP
EGFP-tau-FL
EGFP-tau-AC
AnkG length (µm)
*p = 0.0159
***p = 0.0003
**p = 0.0067
***p < 0.0001
B
βIV-spectrin
EB3
EGFP-tau-FL
EGFP-tau-AC
βIV-spectrin length (µm)
**p = 0.0059
19
26
EB3 length (µm)
**p = 0.0017
13
10
FL
AC
EGFP-tau
C
EGFP-tau-FL
tdTOMATO
AnkG
MERGED
EGFP-tau-AC
Axon / Dendrite ratio
***p < 0.0001
34
28
D
EGFP-tau-FL
EGFP-tau-AC
tdTOMATO
MERGED
Spines with tau / Total spines (%)
** p =0.0111
13
16
# Spines / 50 µm dendrites
p = 0.0977

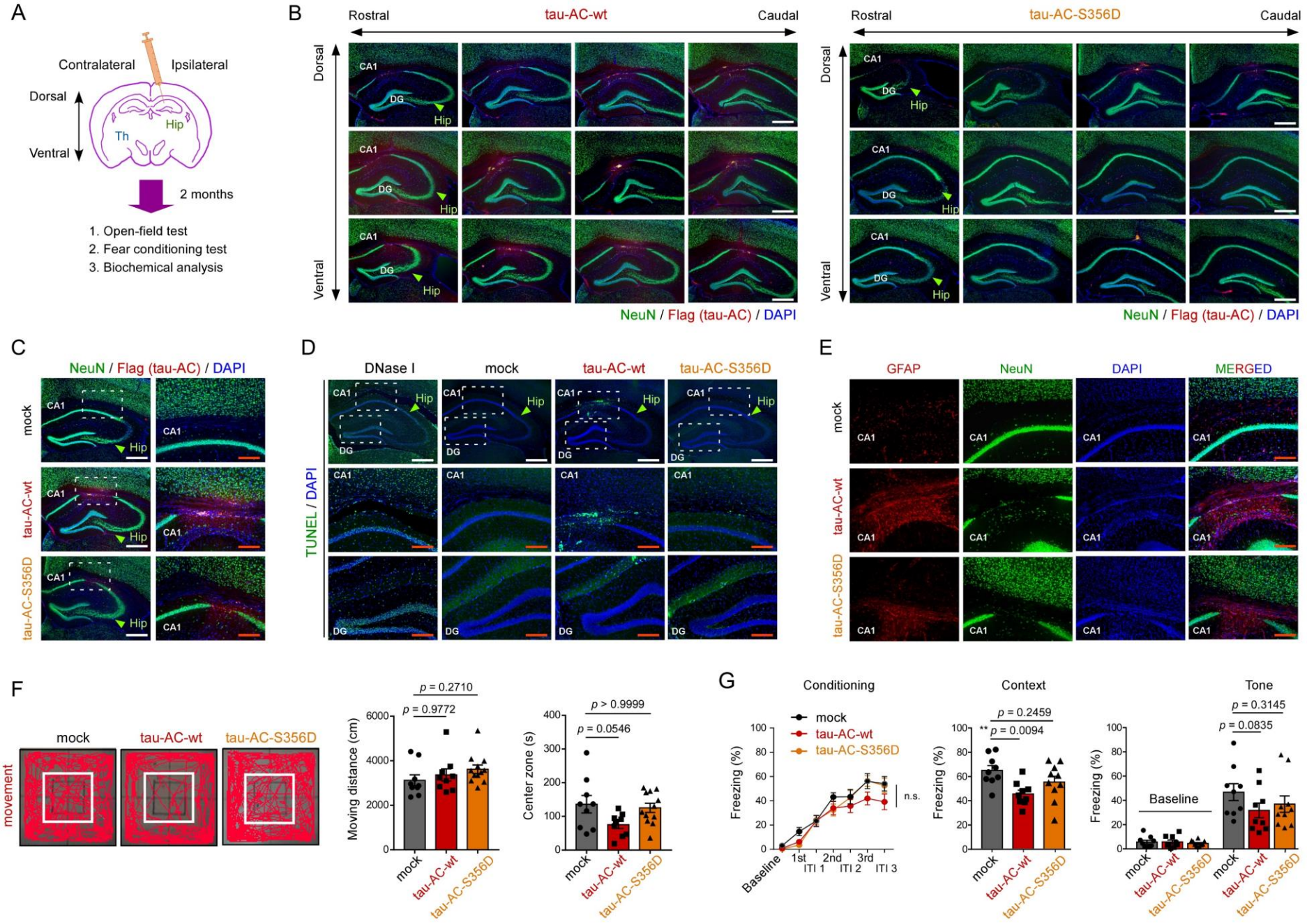
A
Contralateral
Ipsilateral
Dorsal
Ventral
Th
Hip
2 months
1. Open-field test
2. Fear conditioning test
3. Biochemical analysis
B
Rostral
tau-AC-wt
Caudal
Dorsal
Ventral
CA1
DG
Hip
NeuN / Flag (tau-AC) / DAPI
Rostral
tau-AC-S356D
Caudal
C
NeuN / Flag (tau-AC) / DAPI
mock
tau-AC-wt
tau-AC-S356D
D
DNase I
mock
tau-AC-wt
tau-AC-S356D
TUNEL / DAPI
E
GFAP
NeuN
DAPI
MERGED
F
mock
tau-AC-wt
tau-AC-S356D
movement
Moving distance (cm)
p = 0.2710
p = 0.9772
Center zone (s)
p > 0.9999
p = 0.0546
G
Conditioning
Freezing (%)
mock
tau-AC-wt
tau-AC-S356D
n.s.
Baseline
1st
2nd
3rd
ITI 1
ITI 2
ITI 3
Context
p = 0.2459
** p = 0.0094
Tone
p = 0.3145
p = 0.0835
Baseline

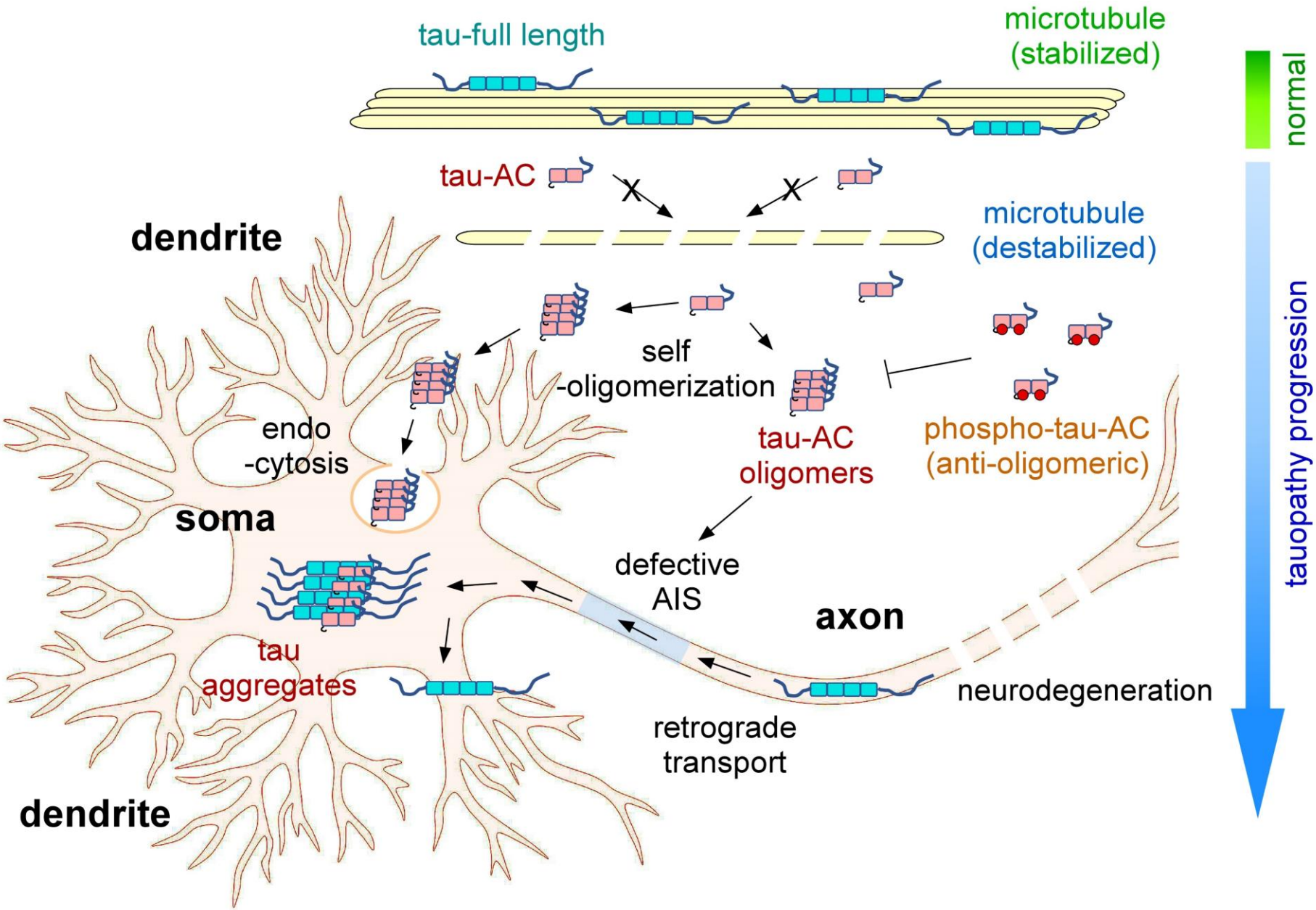
tau-full length
microtubule
(stabilized)
normal
tau-AC
microtubule
(destabilized)
dendrite
self
-oligomerization
endo
-cytosis
tau-AC
oligomers
phospho-tau-AC
(anti-oligomeric)
tauopathy progression
soma
defective
AIS
axon
tau
aggregates
neurodegeneration
retrograde
transport
dendrite